
Empower Structure-Based Molecule Optimization with Gradient Guided Bayesian Flow Networks

Keyue Qiu^{1,2} Yuxuan Song^{1,2} Jie Yu³ Hongbo Ma² Ziyao Cao^{1,2}
Zhilong Zhang⁴ Yushuai Wu¹ Mingyue Zheng³ Hao Zhou¹ Wei-Ying Ma¹

Abstract

Structure-based molecule optimization (SBMO) aims to optimize molecules with both continuous coordinates and discrete types against protein targets. A promising direction is to exert gradient guidance on generative models given their remarkable success in images, but it is challenging to guide discrete data and risks inconsistencies between modalities. To this end, we leverage a continuous and differentiable space derived through Bayesian inference, presenting *Molecule Joint Optimization* (MolJO), the gradient-based SBMO framework that facilitates joint guidance signals across different modalities while preserving SE(3)-equivariance. We introduce a novel backward correction strategy that optimizes within a sliding window of the past, allowing for a seamless trade-off between exploration and exploitation during optimization. MolJO achieves state-of-the-art performance on CrossDocked2020 benchmark (Success Rate 51.3%, Vina Dock -9.05 and SA 0.78), more than 4× improvement in Success Rate compared to the gradient-based counterpart, and 2× “Me-Better” Ratio as high as 3D baselines. Furthermore, we extend MolJO to a wide range of settings, including multi-objective optimization and challenging tasks in drug design such as R-group optimization and scaffold hopping, further underscoring its versatility. Code is available at <https://github.com/AlgoMole/MolCRAFT>.

¹Institute for AI Industry Research (AIR), Tsinghua University
²Department of Computer Science and Technology, Tsinghua University
³Shanghai Institute of Materia Medica, Chinese Academy of Sciences
⁴Peking University. Correspondence to: Hao Zhou <zhouhao@air.tsinghua.edu.cn>.

Proceedings of the 42nd International Conference on Machine Learning, Vancouver, Canada. PMLR 267, 2025. Copyright 2025 by the author(s).

1. Introduction

Structure-based drug design (SBDD) plays a critical role in drug discovery by identifying three-dimensional (3D) molecules that are favorable for protein targets (Iser et al., 2023). While recent SBDD focuses on the initial identification of potential drug candidates, these compounds must undergo a series of further modifications for optimized properties, a process that is both complex and time-consuming (Hughes et al., 2011). Therefore, structure-based molecule optimization (SBMO) has garnered increasing interest in real-world drug design (Zhou et al., 2024a), emphasizing the practical need to optimize for specific therapeutic criteria.

Concretely, SBMO can be viewed as a more advanced task within the broader scope of general SBDD, requiring precise control over molecular properties while navigating the chemical space. Specifically, SBMO addresses two key aspects: (1) *SBMO prioritizes targeted molecular property enhancement according to expert-specified objectives*, while generative models for SBDD focus primarily on maximizing the likelihood of data without special emphasis on property improvement (Luo et al., 2021; Peng et al., 2022). Therefore, these models can only produce outputs similar to their training data, limiting the ability to improve molecular properties. (2) *SBMO is capable of optimizing existing compounds with 3D structural awareness*, addressing a critical gap left by previous molecule optimization methods with 1D SMILES or 2D graph representations (Bilodeau et al., 2022; Fu et al., 2022), and allowing for a more nuanced control. The focus on structure makes SBMO particularly suited for key design tasks, such as R-group optimization and scaffold hopping.

Recent works have explored SBMO through evolutionary-based resampling and gradient-based methods. For instance, DiffSBDD (Schneuing et al., 2022) uses a gradient-free evolutionary sampling method, and DecompOpt (Zhou et al., 2024a) further introduces a fragment-conditioned 3D generative model for resampling. These approaches rely on iterative, computationally expensive oracle calls to select top-of-N candidates. One generalized and orthogonal solution is gradient guidance, eliminating the need for oracle simulations while being flexible enough to be incorporated into strong-performing generative models in a plug-and-play

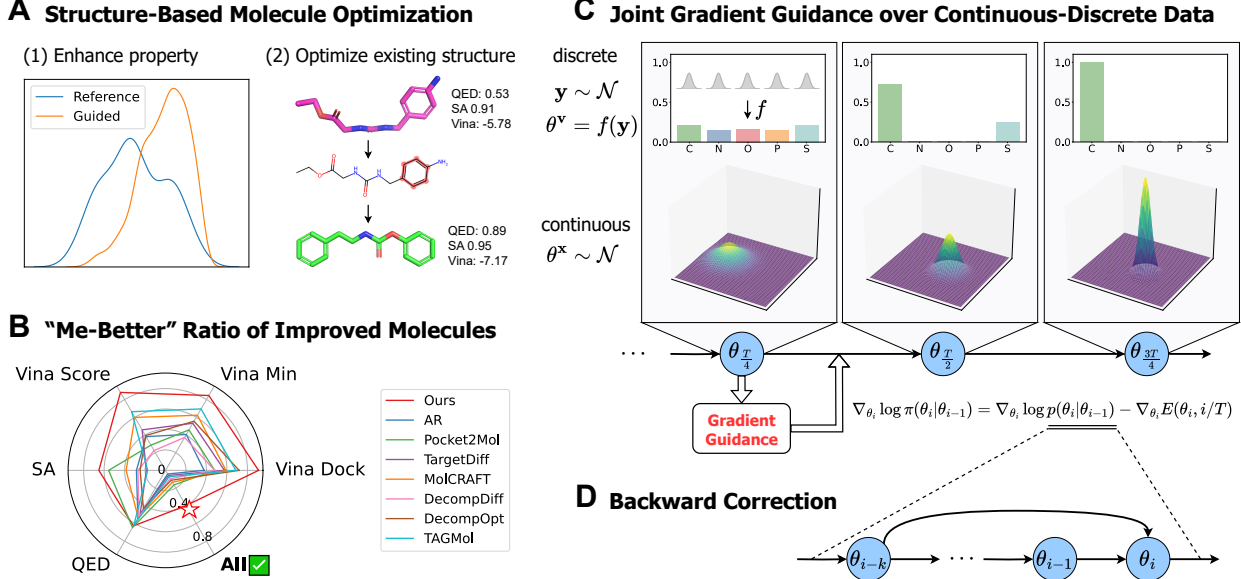


Figure 1. Overview. **A.** Structure-based molecule optimization, including (1) guiding molecule design by expert-specified objectives, (2) optimizing existing compounds in the structure space. **B.** Study on the ratio of “me-better” molecules (with improved properties), where all other baselines fall short in the overall improvement. **C.** Overall illustration of MolJO, utilizing joint gradient signals over continuous-discrete data, where the distributions of θ (for continuous x and discrete v) are taken from true guided trajectories. **D.** Graphical model of our proposed backward correction strategy, keeping a sliding window of size k .

fashion, as demonstrated in a wide range of challenging real-world applications including image synthesis (Dhariwal & Nichol, 2021; Epstein et al., 2023).

However, current gradient-based methods have not fully realized their potential in SBMO, for they have historically suffered from the continuous-discrete challenges: (1) *it is non-trivial to guide discrete variable within probabilistic generative process*. More specifically, standard gradient guidance is designed for continuous variables that follow Gaussian distributions, making them not directly applicable to molecular data that involve discrete atom types. Methods attempting to adapt gradient guidance to discrete data often resort to approximating these variables as continuous, either by adding Gaussian noise (Bao et al., 2022) or by assuming that classifiers follow a Gaussian distribution (Vignac et al., 2023). Unfortunately, these approximations can lead to sub-optimal results, as they do not accurately reflect the discrete nature (Kong et al., 2023). (2) *Gradient guidance might introduce inconsistencies between modalities*. For instance, TAGMol (Dorna et al., 2024) formalizes guidance exclusively over continuous coordinates, resulting in a disconnect between the discrete and continuous modalities. This may explain why TAGMol struggles to optimize overall molecular properties as shown in Fig. 1, despite its improvement in Vina affinities. By solely guiding the continuous coordinates, TAGMol enhances spatial protein-ligand interactions but fails to optimize *e.g.* synthesizability, which depends more on molecular topology, especially discrete atom types.

In this paper, we address the *multi-modality challenge for gradient guidance* by leveraging a continuous and differential space, representing an aggregation of noisy samples from the data space derived through Bayesian inference (Graves et al., 2023). We design MolJO (**M**olecule **J**oint **O**ptimization), a principled, end-to-end differentiable framework that enables gradient-based optimization of continuous and discrete variables. We introduce a novel sampling strategy called backward correction, enhancing the alignment of gradients over different steps. By maintaining a sliding window of past history for optimization, the backward correction strategy enforces explicit dependency on the past, effectively alleviating the issue of inconsistencies. Moreover, it balances the exploration of molecular space with the exploitation of better-aligned guidance signals, offering a flexible trade-off.

Our main contributions are summarized as follows.

- We propose MolJO, the joint gradient-based method for SBMO that establishes the guidance over molecules, offering better controllability and effectively integrating gradient guidance for continuous-discrete variables within a unified framework.
- We design a novel backward correction strategy for effective optimization. By keeping a sliding window and correcting the past given the current optimized version, we achieve better-aligned gradients and facilitate a flexible trade-off between exploration and exploitation.

- MolJO achieves the best Vina Dock of -9.05, SA of 0.78 and Success Rate of 51.3%, and “Me-Better” Ratio of improved molecules that is **$2 \times$ as much as other 3D baselines**. We generalize MolJO to various needs including R-group optimization and scaffold hopping, highlighting its versatility.

2. Related Work

Pocket-Aware Molecule Generation. Pocket-aware generative models aim to learn a conditional distribution over the protein-ligand complex data. Initial approaches adopt 1D SMILES or 2D graph representation (Bjerrum & Threlfall, 2017; Gómez-Bombarelli et al., 2018), and recent research has shifted its focus towards 3D molecule generation in order to better capture interatomic interactions. Early atom-based autoregressive models (Luo et al., 2021; Peng et al., 2022; Liu et al., 2022) enforce an atom ordering to generate molecules atom-by-atom. Fragment-based methods (Powers et al., 2022; Zhang et al., 2023; Lin et al., 2023) alleviate the issue of ordering by decomposing molecules into motifs instead of atom-level generation, but they risk more severe error accumulation and thus generally require post-processing or multi-stage treatment. Non-autoregressive methods based on diffusions (Schneuring et al., 2022; Guan et al., 2022; 2023) and BFNs (Qu et al., 2024) target full-atom generation for enhanced performance and efficiency. However, the needs of optimizing certain properties and modifying existing compounds are not adequately addressed in the scope of previous methods, limiting their usefulness in drug design.

Gradient-Based Molecule Optimization. Inspired by classifier guidance for diffusions (Dhariwal & Nichol, 2021), pioneering approaches are committed to adapting the guidance method to handle the complicated molecular geometries in the setting of pocket-unaware generation. EEGSDE (Bao et al., 2022) derives an equivariant framework for continuous diffusion, and MUDM (Han et al., 2023) further explores time-independent property functions for guidance. As they enforce a continuous diffusion process for discrete variables, these methods are not applicable in advanced molecular modeling (Guan et al., 2022; 2023) where discrete data are processed by a discrete diffusion, for it is unnatural to apply progressive Gaussian noise that drives Categorical data away from the simplex. DiGress (Vignac et al., 2023) proposes classifier guidance for discrete diffusion of molecular graphs, yet it additionally assumes that the probability of classifier follows a Gaussian, which is ungrounded and often a problematic approximation. Based on the continuous-discrete diffusion for SBDD, TAGMol (Dorna et al., 2024) retains the guidance only for continuous coordinates, because there lacks a proper way to propagate the gradient over discrete types. The discrete part is affected

only implicitly and belatedly in the generative process, and such imbalanced guidance would probably result in suboptimal performance for lack of joint optimization.

3. Preliminary

3D Protein-Ligand Representation. A protein binding site $\mathbf{p} = (\mathbf{x}_P, \mathbf{v}_P)$ is represented as a point cloud of N_P atoms with coordinates $\mathbf{x}_P = \{\mathbf{x}_P^1, \dots, \mathbf{x}_P^{N_P}\} \in \mathbb{R}^{N_P \times 3}$ and K_P -dimensional atom features $\mathbf{v}_P = \{\mathbf{v}_P^1, \dots, \mathbf{v}_P^{N_P}\} \in \mathbb{R}^{N_P K_P}$. Similarly, a ligand molecule $\mathbf{m} = (\mathbf{x}_M, \mathbf{v}_M)$ contains N_M atoms, where $\mathbf{x}_M^{(i)} \in \mathbb{R}^3$ is the atomic coordinate and $\mathbf{v}_M^{(i)} \in \mathbb{R}^{K_M}$ the atom type. For brevity, the subscript for molecules \cdot_M and the pocket condition \mathbf{p} are omitted unless necessary.

Bayesian Flow Networks (BFNs). We briefly introduce how BFN views the generative modeling as message exchange between a sender and a receiver, with more details in Appendix A. The *sender distribution* $p_S(\mathbf{y} | \mathbf{x}; \alpha)$ builds upon the accuracy level α applied to data \mathbf{x} and defines the noised \mathbf{y} . The varying noise levels constitute the schedule $\beta(t) = \int_{t'=0}^t \alpha(t') dt'$, similar to that in diffusion models.

A key motivation for BFN is that the transmission ought to be continuous and smooth, therefore it does not directly operate on the noisy latent \mathbf{y} as diffusions, but on the structured Bayesian posterior θ given noisy latents instead. The receiver holds a prior belief θ_0 , and updates the belief upon observed \mathbf{y} , yielding the *Bayesian update distribution*:

$$p_U(\theta_i | \theta_{i-1}, \mathbf{x}; \alpha_i) = \mathbb{E}_{p_S(\mathbf{y}_i | \mathbf{x}; \alpha_i)} \delta(\theta_i - h(\theta_{i-1}, \mathbf{y}_i, \alpha_i)) \quad (1)$$

where $\delta(\cdot)$ is Dirac distribution, and Bayesian update function h is derived through Bayesian inference.

Intuitively, BFN aims to predict the clean sample given aggregated θ , i.e. conditioning on all previous latents. θ is fed into a neural network Φ to estimate the distribution of clean datapoint $\hat{\mathbf{x}}$, i.e. the *output distribution* $p_O(\hat{\mathbf{x}} | \Phi(\theta, t))$. The *receiver distribution* is obtained by marginalizing out $\hat{\mathbf{x}}$:

$$p_R(\mathbf{y}_i | \theta_{i-1}; t_i, \alpha_i) = \mathbb{E}_{p_O(\hat{\mathbf{x}} | \Phi(\theta_{i-1}, t_i))} p_S(\mathbf{y}_i | \hat{\mathbf{x}}; \alpha_i) \quad (2)$$

The training objective is to minimize the KL-divergence between sender and receiver distributions:

$$L^n(\mathbf{x}) = \mathbb{E}_{\prod_{i=1}^n p_U(\theta_i | \theta_{i-1}, \mathbf{x}; \alpha_i)} \sum_{i=1}^n D_{KL}(p_S(\mathbf{y}_i | \mathbf{x}; \alpha_i) \| p_R(\mathbf{y}_i | \theta_{i-1}, t_i, \alpha_i)). \quad (3)$$

4. Method

In this section, we introduce MolJO that guides the distribution over θ , utilizing aggregated information from previous

latents. Though different from guided diffusions that operate on noisy latent \mathbf{y} , this guidance aligns with our generative process informed by θ . By focusing on lower-variance θ , we can effectively steer the clean samples towards desirable direction, ensuring a smooth gradient flow.

Notation. Following Kong et al. (2024) and denoting the guided distribution π as product of experts (Hinton, 2002) modulated by energy function E that predicts certain property, we have $\pi(\theta_i|\theta_{i-1}) \propto p_\phi(\theta_i|\theta_{i-1})p_E(\theta_i)$, where Φ is the pretrained network for BFN, $p_E(\theta_i) = \exp[-E(\theta_i, t_i)]$ is the unnormalized Boltzmann distribution corresponding to the time-dependent energy function.

Overview. As illustrated in Fig. 1, we introduce MolJO as follows: in Sec. 4.1, we propose the concept of gradient guidance over the multi-modality molecule space, derive the form of guided transition kernel $\pi(\theta_i|\theta_{i-1})$ via first-order Taylor expansion, and explain the underlying manipulations of distributions the guidance corresponds to. In Sec. 4.2, we present a generalized advanced sampling strategy termed backward correction for p_ϕ , which allows for a flexible trade-off between explore-and-exploit by maintaining a sliding window of past histories. We empirically demonstrate our strategy helps optimize consistency across steps, ultimately improving the overall performance.

4.1. Equivariant Guidance for multi-modality Molecular Data

In this section, we derive the detailed guidance over θ for molecule $\mathbf{m} = (\mathbf{x}, \mathbf{v})$ with N atoms, where $\mathbf{x} \in \mathbb{R}^{N \times 3}$ represent continuous atom coordinates and $\mathbf{v} \in \{1, \dots, K\}^N$ for K discrete atom types, and thus $\theta := [\theta^x, \theta^v]$, latent $\mathbf{y} := [\mathbf{y}^x, \mathbf{y}^v]$ for the continuous and discrete modality.

Guidance over Multi-Modalities. To steer the sampling process towards near-optimal samples, we utilize the score $\nabla_\theta \log p_E(\theta)$ as a gradient-based property guidance, for which we have the following proposition (proof in Appendix C.1), followed by details for each modality.

Proposition 4.1. Suppose $\tilde{\theta}_i^x \sim \mathcal{N}(\theta_\phi^x, \sigma^x \mathbf{I})$ and $\tilde{\mathbf{y}}_i \sim \mathcal{N}(\mathbf{y}_\phi, \sigma^x \mathbf{I})$ by definition of BFN generative process, we can approximate the guided transition kernel $\pi(\theta_i|\theta_{i-1})$:

$$\theta_i^x \sim \mathcal{N}(\theta_\phi^x + \sigma^x \mathbf{g}_{\theta^x}, \sigma^x \mathbf{I}) \quad (4)$$

$$\mathbf{y}_i^v \sim \mathcal{N}(\mathbf{y}_\phi^v + \sigma^v \mathbf{g}_{\theta^v}, \sigma^v \mathbf{I}) \quad (5)$$

where gradient $\mathbf{g}_{\theta^x} = -\nabla_{\theta^x} E(\theta, t_i)|_{\theta=\theta_{i-1}}$, $\mathbf{g}_{\theta^v} = -\nabla_{\theta^v} E(\theta, t_i)|_{\theta=\theta_{i-1}}$, $\mathbf{g}_{\mathbf{y}^v} = \mathbf{g}_{\theta^v} \frac{\partial \theta^v}{\partial \mathbf{y}^v}$.

The guidance is formalized over both continuous coordinates and discrete types, and differs from previous guided diffusion for molecules in that (1) it guides the discrete data

through Gaussian-distributed latent \mathbf{y} and ensures that the discrete variables are still on the probability simplex without relying on assumptions (Vignac et al., 2023) or relaxations (Bao et al., 2022; Han et al., 2023), and (2) alleviates the inconsistencies between modalities (Dorna et al., 2024) by joint gradient signals.

Guiding θ^x for Continuous \mathbf{x} . For continuous coordinates $\mathbf{x} \in \mathbb{R}^{N \times 3}$, it is natural to adopt a Gaussian sender distribution $\mathbf{y}^x \sim \mathcal{N}(\mathbf{x}, \alpha^{-1} \mathbf{I})$. With a prior belief $\theta_0^x = 0$, we have the Bayesian update function for posterior θ_i^x given noisy \mathbf{y}^x as in Graves et al. (2023):

$$h(\theta_{i-1}^x, \mathbf{y}^x, \alpha_i) = \frac{\theta_{i-1}^x \rho_{i-1} + \mathbf{y}^x \alpha_i}{\rho_i} \quad (6)$$

with $\alpha_i = \beta_i^x - \beta_{i-1}^x$, $\rho_i = 1 + \beta_i^x$ given the schedule $\beta_i^x = \sigma_1^{-2i/n} - 1$ for a positive σ_1 and n steps.

Remark 4.2. In the continuous domain, guidance over θ^x is analogous to guided diffusions, since guiding θ^x corresponds to guiding noisy latent \mathbf{y}^x using the uncertainty-adjusted gradient $(\frac{\rho_i}{\alpha_i})^2 \mathbf{g}_{\mathbf{y}^x}$ that accounts for how changes in the sample space \mathbf{y}^x propagate to parameter space θ^x :

$$\begin{aligned} \theta_i^x &= \tilde{\theta}_i^x + \sigma^x \mathbf{g}_{\theta^x} \\ &= \frac{\theta_{i-1}^x \rho_{i-1} + (\tilde{\mathbf{y}}^x + \sigma^x \frac{\rho_i}{\alpha_i} \mathbf{g}_{\theta^x}) \alpha_i}{\rho_i} \\ &= \frac{\theta_{i-1}^x \rho_{i-1} + (\tilde{\mathbf{y}}^x + \sigma^x (\frac{\rho_i}{\alpha_i})^2 \mathbf{g}_{\mathbf{y}^x}) \alpha_i}{\rho_i} \end{aligned} \quad (7)$$

Guiding θ^v for Discrete \mathbf{v} . For N -dimensional discrete types $\mathbf{v} \in \{1, \dots, K\}^N$, the noisy latent represents the counts of each type among K types, where we have $\mathbf{y}^v \sim \mathcal{N}(\mathbf{y}^v | \alpha(K\mathbf{e}_v - \mathbf{1}), \alpha K \mathbf{I})$, $\mathbf{e}_v = [\mathbf{e}_{v^{(1)}}, \dots, \mathbf{e}_{v^{(N)}}] \in \mathbb{R}^{KN}$, $\mathbf{e}_{v^{(j)}} = \delta_{v^{(j)}} \in \mathbb{R}^K$ with Kronecker delta function δ . Further explanation is left to Appendix B.

θ_i^v as a posterior belief is updated from the prior $\theta_0^v = \frac{1}{K}$:

$$h(\theta_{i-1}^v, \mathbf{y}^v, \alpha_i) = \frac{\exp(\mathbf{y}^v) \theta_{i-1}^v}{\sum_{k=1}^K \exp(\mathbf{y}_k^v) (\theta_{i-1}^v)_k} \quad (8)$$

where the redundant $\alpha_i = \beta_i^v - \beta_{i-1}^v$ with $\beta_i^v = \beta_1^v (\frac{i}{n})^2$, given a positive hyperparameter β_1^v .

Remark 4.3. In the discrete domain, guiding all latents \mathbf{y}^v amounts to a reweight of the Categorical distribution for θ^v , changing the probability of each class in accordance with the gradient. Take an extreme case to illustrate, where $\mathbf{g}_{\mathbf{y}^v}$ is filled with one-hot vectors δ_d :

$$\begin{aligned} (\theta_i^v)_k &= \frac{\exp(\tilde{\mathbf{y}}_k^v) (\theta_{i-1}^v)_k}{\sum_l \exp(\tilde{\mathbf{y}}_l^v) (\theta_{i-1}^v)_l + [\exp(\sigma^v) - 1] \exp(\tilde{\mathbf{y}}_d^v) (\theta_{i-1}^v)_d} \\ &= (\tilde{\theta}_i^v)_k \frac{1}{1 + C} < (\tilde{\theta}_i^v)_k \end{aligned} \quad (9)$$

for all $k \neq d$, where $C = \frac{[\exp(\sigma^v) - 1] \exp(\tilde{\mathbf{y}}_d^v) (\boldsymbol{\theta}_{i-1}^v)_d}{[\sum_{l=1}^K \exp(\tilde{\mathbf{y}}_l^v)]} > 0$ as the variance $\sigma^v > 0$. It is obvious that the guidance lowers the probability for all classes but the favored d , redistributing the mass for discrete data in a more structured way than diffusion counterparts.

Equivariance. Our proposed guided sampling that utilizes joint gradient signals is still equivariant as shown in the proposition below, with the proof in Appendix C.2.

Proposition 4.4. *The guided sampling process preserves SE(3)-equivariance when Φ is SE(3)-equivariant, if the energy function $E(\boldsymbol{\theta}, \mathbf{p}, t)$ is also SE(3)-equivariant and the complex is shifted to the space where the protein's Center of Mass (CoM) is zero.*

4.2. Bayesian Update With Backward Correction

Algorithm 1 Gradient Guided Sampling of MolJO

Require: network $\Phi(\boldsymbol{\theta}, t, \mathbf{p})$, schedules $[\beta^x(t), \beta^v(t)]$, number of sample steps n , back correction steps k , number of atom types K , energy function $E(\boldsymbol{\theta}, \mathbf{p}, t)$, guidance scale s

- 1: Initialize belief $\boldsymbol{\theta} := [\boldsymbol{\theta}^x, \boldsymbol{\theta}^v] \leftarrow [\mathbf{0}, \frac{1}{K}]$
- 2: **for** $i = 1$ to n **do**
- 3: $[t, t_{-k}] \leftarrow [\frac{i-1}{n}, \max(0, \frac{i-k-1}{n})]$
- 4: $[\hat{\mathbf{x}}, \hat{\mathbf{e}}_v] \leftarrow \Phi(\boldsymbol{\theta}, t, \mathbf{p})$
- 5: $[\mathbf{g}_{\boldsymbol{\theta}^x}, \mathbf{g}_{\boldsymbol{\theta}^v}] \leftarrow [-\nabla_{\boldsymbol{\theta}^x} E(\boldsymbol{\theta}, \mathbf{p}, t), -\nabla_{\boldsymbol{\theta}^v} E(\boldsymbol{\theta}, \mathbf{p}, t)]$
- 6: $[\rho, \rho_{-k}, \Delta\beta^x, \Delta\beta^v] \leftarrow [1 + \beta^x(t), 1 + \beta^x(t_{-k}), \beta^x(t) - \beta^x(t_{-k}), \beta^v(t) - \beta^v(t_{-k})]$
- 7: Retrieve $\boldsymbol{\theta}_{-k}^x, \boldsymbol{\theta}_{-k}^v$ from the past
- 8: Sample $\boldsymbol{\theta}^x$ according to Eq. 4 and 13
- 9: Sample \mathbf{y}^v and update $\boldsymbol{\theta}^v$ according to Eq. 5 and 14
- 10: **end for**
- 11: $[\hat{\mathbf{x}}, \hat{\mathbf{e}}_v] \leftarrow \Phi(\boldsymbol{\theta}, 1, \mathbf{p})$
- 12: $\hat{\mathbf{v}} \leftarrow \arg \max(\hat{\mathbf{e}}_v)$
- 13: **return** $[\hat{\mathbf{x}}, \hat{\mathbf{v}}]$

Here we propose a general backward correction sampling strategy inspired from the optimization perspective, and analyze its effect on aligning the gradients. Recall that from Eq. 1 we can aggregate $\boldsymbol{\theta}_i$ from previous latents:

$$p_\phi(\boldsymbol{\theta}_i | \boldsymbol{\theta}_{i-1}) = \mathbb{E}_{p_O(\hat{\mathbf{x}}_i | \Phi(\boldsymbol{\theta}_{i-1}, t_i))} p_U(\boldsymbol{\theta}_i | \boldsymbol{\theta}_{i-1}, \hat{\mathbf{x}}_i; \alpha_i) \quad (10)$$

Backward correction aims at “correcting the past to further optimize”. Since we obtain an optimized $\boldsymbol{\theta}_i^*$ from the guided kernel $\pi(\boldsymbol{\theta}_i | \boldsymbol{\theta}_{i-1})$, there will be an optimized version of $\hat{\mathbf{x}}_i^* = \hat{\mathbf{x}}_{i+1}$ for the next step. By backward correcting the Bayesian update distribution p_U given the optimized $\hat{\mathbf{x}}^*$, we are able to reinforce the current best possible parameter $\boldsymbol{\theta}$, instead of building on the suboptimal history. By utilizing

the property of additive accuracy once p_U follows certain form as described by Graves et al. (2023), the one-step backward correction can be derived as follows:

$$\begin{aligned} p_\phi(\boldsymbol{\theta}_i | \boldsymbol{\theta}_{i-1}, \boldsymbol{\theta}_{i-2}) &= \\ \mathbb{E}_{p_O(\hat{\mathbf{x}}_i | \Phi(\boldsymbol{\theta}_{i-1}, t_i))} \mathbb{E}_{p_U(\boldsymbol{\theta}_{i-1} | \boldsymbol{\theta}_{i-2}, \hat{\mathbf{x}}_i; \alpha_{i-1})} p_U(\boldsymbol{\theta}_i | \boldsymbol{\theta}_{i-1}, \hat{\mathbf{x}}_i; \alpha_i) \\ &= \mathbb{E}_{p_O(\hat{\mathbf{x}}_i | \Phi(\boldsymbol{\theta}_{i-1}, t_i))} p_U(\boldsymbol{\theta}_i | \boldsymbol{\theta}_{i-2}, \hat{\mathbf{x}}_i; \alpha_{i-1} + \alpha_i) \end{aligned} \quad (11)$$

where the original $\hat{\mathbf{x}}_{i-1} \sim p_O(\hat{\mathbf{x}}_{i-1} | \Phi(\boldsymbol{\theta}_{i-2}, t_{i-1}))$ that has been used to update $\boldsymbol{\theta}_{i-1}$ from $\boldsymbol{\theta}_{i-2}$ at previous step, is now replaced by the optimized $\hat{\mathbf{x}}_i$. By iteratively tracing back, we arrive at the $k-1$ step corrected estimation of p_ϕ :

$$\begin{aligned} p_\phi(\boldsymbol{\theta}_n | \boldsymbol{\theta}_{n-1}, \boldsymbol{\theta}_{n-k}) &= \\ \mathbb{E}_{p_O(\hat{\mathbf{x}}_n | \Phi(\boldsymbol{\theta}_{n-1}, t_n))} p_U(\boldsymbol{\theta}_n | \boldsymbol{\theta}_{n-k}, \hat{\mathbf{x}}_n; \sum_{i=n-k+1}^n \alpha_i) \end{aligned} \quad (12)$$

Plugging Eq. 6 and 8 together with the sender distributions defined above into the right hand side according to Eq. 1, yields the form of the backward corrected Bayesian update

$$p_U(\boldsymbol{\theta}_n^x | \boldsymbol{\theta}_{n-k}^x, \hat{\mathbf{x}}_n) = \mathcal{N}\left(\frac{\Delta\beta\hat{\mathbf{x}}_n + \boldsymbol{\theta}_{n-k}^x \rho_{n-k}}{\rho_n}, \frac{\Delta\beta}{\rho_n^2} \mathbf{I}\right) \quad (13)$$

$$\begin{aligned} p_U(\boldsymbol{\theta}_n^v | \boldsymbol{\theta}_{n-k}^v, \hat{\mathbf{v}}_n) &= \mathbb{E}_{\mathbf{y} \sim \mathcal{N}(\mathbf{y} | \Delta\beta^v(K\mathbf{e}_{\hat{\mathbf{v}}_n} - \mathbf{1}), \Delta\beta^v K\mathbf{I})} \\ &\quad \delta\left(\boldsymbol{\theta}_n^v - \frac{\exp(\mathbf{y})\boldsymbol{\theta}_{n-k}^v}{\sum_{i=1}^K \exp(\mathbf{y}_i)(\boldsymbol{\theta}_{n-k}^v)_i}\right) \end{aligned} \quad (14)$$

where $\hat{\mathbf{m}} = [\hat{\mathbf{x}}, \hat{\mathbf{v}}]$ is drawn from the output distribution $p_O(\hat{\mathbf{m}} | \Phi(\boldsymbol{\theta}_{i-1}, t_{i-1}, \mathbf{p}))$ given pocket \mathbf{p} , $\Delta\beta^x = \beta_n^x - \beta_{n-k}^x$ and $\Delta\beta^v = \beta_n^v - \beta_{n-k}^v$ are obtained from corresponding accuracy schedules. The concept of sliding window unifies different sampling strategies proposed by Graves et al. (2023) ($k=1$) and Qu et al. (2024) ($k=n$). To understand its effect, we visualize the cosine similarity of gradients at each step w.r.t. the previous step in Fig. 2. By changing the size k of sliding window, it succeeds in balancing sample quality (*explore*) and optimization efficiency (*exploit*), where it first focuses on exploring the molecular space with rapidly changing structures and gradients, and then exploits better-aligned guidance signals over gradually refined structures.

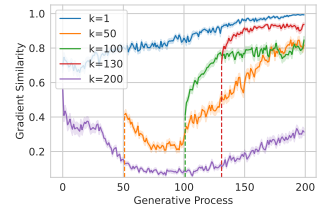


Figure 2. Gradient cosine similarity, where k denotes the backward correction window size. For $1 < k < 200$, the similarity before timestep k is omitted for it overlaps with $k = 200$, i.e. covering all the past.

In practice, we employ the gradient scale s as a temperature parameter, equivalent to $p_E^s(\theta, t) \propto \exp[-sE(\theta, t)]$. We further bypass the derivative $\frac{\partial \theta^v}{\partial y^v} = \theta^v(1 - \theta^v)$ to stabilize the gradient flow. The general sampling procedure is summarized in Algorithm 1.

5. Experiments

5.1. Experimental Setup

We conduct two sets of experiments for structure-based molecule optimization (SBMO), although the constrained setting seems within the scope of unconstrained one, it is biologically meaningful and more practical in rational drug design, and further showcases the flexibility of our method.

Task. For a molecule $\mathbf{m} \in \mathcal{M}$ where \mathcal{M} denotes the set of molecules, there are oracles $a_i(\mathbf{m}) : \mathcal{M} \rightarrow \mathbb{R}$ for property i , each with a desired threshold $\delta_i \in \mathbb{R}$. MolJO is capable of different levels of controllability: (1) unconstrained optimization, where we identify a set of molecules such that $\{\mathbf{m} \in \mathcal{M} \mid a_i(\mathbf{m}) \geq \delta_i, \forall i\}$, *i.e.* the goal is to optimize a number of objectives. (2) constrained optimization, where we aim to find a set of molecules that contain specific substructures s such that $\{\mathbf{m} \in \mathcal{M} \mid a_i(\mathbf{m}) \geq \delta_i, s \subset \mathbf{m}, \forall i\}$.

Dataset. Following previous SBDD works (Luo et al., 2021), we utilize CrossDocked2020 (Francoeur et al., 2020) to train and test our model, and adopt the same processing that filters out poses with $\text{RMSD} > 1\text{\AA}$ and clusters proteins based on 30% sequence identity, yielding 100,000 training poses and 100 test proteins.

Baselines. We divide all baselines into the following: (1) Generative models (*Gen*), including AR (Luo et al., 2021), GraphBP (Liu et al., 2022), Pocket2Mol (Peng et al., 2022), FLAG (Zhang et al., 2023), DiffSBDD (Schneuing et al., 2022), TargetDiff (Guan et al., 2022), DecompDiff (Guan et al., 2023), IPDiff (Huang et al., 2024) and MolCRAFT (Qu et al., 2024), (2) Oracle-based optimization (*Oracle*) that rely on docking simulation in each round, such as AutoGrow4 (Spiegel & Durrant, 2020), RGA (Fu et al., 2022), and DecompOpt (Zhou et al., 2024a), (3) Gradient-guided (*Grad*) TAGMol (Dorna et al., 2024). Detailed descriptions of baselines are left in Appendix F.

Metrics. We employ the commonly used metrics as follows: (1) Affinity metrics calculated by Autodock Vina (Eberhardt et al., 2021), in which **Vina Score** calculates the raw energy of the given molecular pose residing in the pocket, **Vina Min** conducts a quick local energy minimization and scores the minimized pose, and **Vina Dock** performs a relatively longer search for optimal pose to calculate the lowest energy. **Success Rate** measures the percentage of

generated molecules that pass certain criteria (Vina Dock < -8.18 , QED > 0.25 , SA > 0.59) following Guan et al. (2022). (2) Molecular properties, including drug-likeness (**QED**) and synthesizability score (**SA**). (3) Metrics for sample distribution, such as diversity (**Div**). A more comprehensive set of metrics are detailed in Appendix F.

5.2. Unconstrained Optimization

In this section, we demonstrate the ability of our framework to improve molecular properties in both single and multi-objective optimization. We sample 100 molecules for each protein and evaluate MolJO in optimizing binding affinity and molecular properties. For additional evaluation of molecular conformation besides optimization performance, please see Appendix G.

MolJO effectively enhances molecular property w.r.t. generative models. The optimized distribution greatly improves upon the original generated distribution, as shown in Table 1 (row 14 *vs.* row 9).

MolJO outperforms gradient-based method with 4 \times higher Success Rate. As shown in Table 1, our model achieves state-of-the-art in affinity-related metrics while being highly drug-like, with the best Success Rate of 51.3%, a four-fold improvement over TAGMol (row 14 *vs.* row 13).

MolJO has more potential than oracle-based baselines if equipped with oracles. RGA (Fu et al., 2022) and DecompOpt (Zhou et al., 2024a) show satisfactory Success Rate, enjoying the advantage of oracle-based screening at some expense of diversity, while AutoGrow4 (Spiegel & Durrant, 2020) falls short in QED, yielding a suboptimal Success Rate. Given the same concentration use of Z-score (Zhou et al., 2024a), we report a variant of MolJO with top-of- N , selecting a tenth of top scoring molecules and showing that it is more effective than oracle-based methods once in a similar setting. Moreover, the higher diversity of DecompOpt and MolJO suggests the superiority of 3D structure-aware generative models over 2D optimization baselines (row 15 *vs.* row 10-12).

MolJO is 2 \times as effective in proposing “me-better” candidates. For gradient-based method TAGMol (Dorna et al., 2024), although it produces seemingly promising high affinity binders, they come at the expense of sacrificed molecular properties like QED and SA, demonstrating the suboptimal control of coordinate-only guidance signals. Notably, the ratio of all-better samples is below 17% for all other baselines, and MolJO is twice as effective (39.8%) in generating feasible drug candidates that pass this criteria (Fig. 1).

Table 1. Summary of different properties of reference molecules and generated molecules by our model and other baselines, where G+O denotes equipping our method with top-of- N in oracle simulations. Additional baselines and results can be found in Appendix F.1. (\uparrow) / (\downarrow) denotes a larger / smaller number is better. Top 2 results are highlighted with **bold text** and underlined text.

Methods	Vina Score (\downarrow)		Vina Min (\downarrow)		Vina Dock (\downarrow)		QED (\uparrow)		SA (\uparrow)		Div (\uparrow)		Success Rate (\uparrow)
	Avg.	Med.	Avg.	Med.	Avg.	Med.	Avg.	Med.	Avg.	Med.	Avg.	Med.	
Reference	-6.36	-6.46	-6.71	-6.49	-7.45	-7.26	0.48	0.48	0.73	-	-	-	25.0%
Gen	① AR	-5.75	-5.64	-6.18	-5.88	-6.75	-6.62	0.51	0.63	0.70	0.70	6.9%	
	② GraphBP	-	-	-	-	-4.80	-4.70	0.43	0.49	0.79	0.79	0.1%	
	③ Pocket2Mol	-5.14	-4.70	-6.42	-5.82	-7.15	-6.79	0.57	0.76	0.69	0.69	24.4%	
	④ FLAG	45.85	36.52	9.71	-2.43	-4.84	-5.56	<u>0.61</u>	0.63	0.70	0.70	1.8%	
	⑤ DiffSBDD	-1.44	-4.91	-4.52	-5.84	-7.14	-7.30	0.47	0.58	0.73	0.73	7.9%	
	⑥ TargetDiff	-5.47	-6.30	-6.64	-6.83	-7.80	-7.91	0.48	0.58	0.72	0.72	10.5%	
	⑦ DecompDiff	-5.19	-5.27	-6.03	-6.00	-7.03	-7.16	0.51	0.66	0.73	0.73	14.9%	
	⑧ IPDiff	-6.41	-7.01	-7.45	-7.48	-8.57	-8.51	0.52	0.59	0.74	0.74	16.5%	
	⑨ MolCRAFT	-6.55	-6.95	-7.21	-7.14	-7.67	-7.82	0.50	0.67	0.70	0.70	26.8%	
Oracle	⑩ AutoGrow4	-	-	-	-	-8.99	-9.00	0.46	0.76	0.47	0.47	14.3%	
	⑪ RGA	-	-	-	-	-8.01	-8.17	0.57	0.71	0.41	0.41	46.2%	
	⑫ DecompOpt	-5.75	-5.97	-6.58	-6.70	-7.63	-8.02	0.56	0.73	0.63	0.63	39.4%	
Grad	⑬ TAGMol	-7.02	-7.77	-7.95	-8.07	-8.59	-8.69	0.55	0.56	0.69	0.69	11.1%	
	⑭ MolJO	<u>-7.52</u>	<u>-8.02</u>	<u>-8.33</u>	<u>-8.34</u>	<u>-9.05</u>	<u>-9.13</u>	0.56	<u>0.78</u>	0.66	<u>0.66</u>	<u>51.3%</u>	
G + O	⑮ MolJO [†] (N=10)	-8.54	-8.81	-9.48	-9.09	-10.50	-10.14	0.67	0.79	0.61	0.70	70.3%	

Table 2. Constrained optimization results, where *Redesign* means R-group optimization with fragments of the same size redesigned, *Growing* means fragment growing into larger size, *Hopping* means scaffold hopping.

Methods	Vina Score (\downarrow)		Vina Min (\downarrow)		Vina Dock (\downarrow)		QED (\uparrow)		SA (\uparrow)		Connected		Success Rate (\uparrow)
	Avg.	Med.	Avg.	Med.	Avg.	Med.	Avg.	Med.	Avg.	Med.	Avg.	Med.	
Reference	-6.36	-6.46	-6.71	-6.49	-7.45	-7.26	0.48	0.48	0.73	-	100%	-	25.0%
Redesign	TargetDiff	-6.14	-6.21	-6.79	-6.58	-7.70	-7.61	0.50	0.64	85.5%	85.5%	18.9%	
	TAGMol	-6.60	-6.66	-7.10	-6.80	-7.63	-7.76	0.53	0.62	87.0%	87.0%	19.2%	
	MolCRAFT	-6.63	-6.70	-7.12	-6.91	-7.79	-7.72	0.49	0.67	96.7%	96.7%	22.7%	
	MolJO	-7.13	-7.28	-7.62	-7.39	-8.16	-8.20	0.57	0.68	95.1%	95.1%	29.0%	
Growing	TargetDiff	-6.73	-7.29	-7.60	-7.67	-8.89	-8.79	0.39	0.52	71.6%	71.6%	11.2%	
	TAGMol	-7.30	-7.70	-8.08	-7.81	-8.92	-8.78	0.47	0.53	78.7%	78.7%	11.8%	
	MolCRAFT	-6.96	-7.47	-7.86	-7.73	-8.80	-8.65	0.44	0.59	91.7%	91.7%	19.9%	
	MolJO	-8.08	-8.35	-8.79	-8.58	-9.21	-9.45	0.53	0.62	93.2%	93.2%	32.7%	
Hopping	TargetDiff	-5.72	-5.78	-6.00	-5.83	-6.31	-6.66	0.39	0.65	63.3%	63.3%	6.2%	
	TAGMol	-6.17	-6.10	-6.46	-6.07	-7.19	-6.80	0.44	0.62	68.7%	68.7%	6.9%	
	MolCRAFT	-6.31	-6.17	-6.58	-6.40	-7.25	-7.15	0.42	0.67	89.9%	89.9%	14.6%	
	MolJO	-6.86	-6.50	-7.13	-6.70	-7.67	-7.58	0.46	0.68	90.5%	90.5%	23.6%	

MolJO excels even in optimizing large OOD molecules. Note that for fair comparison, we restrict the size of generated molecules by reference molecules so that both generative models and optimization methods navigate the similar chemical space, as we observe a clear correlation between properties and sizes in Fig. 4. For model variants capable of exploring larger number of atoms, we report the results in Table 3 with sizes, where MolJO consistently outperforms other baselines, demonstrating its robustness. A detailed discussion can be found in Appendix E.

5.3. Constrained Optimization

Constrained optimization seeks to optimize the input reference molecules for enhanced properties while retaining specific structures. We generalize our framework with such structural control and show its potential for pharmaceuti-

Table 3. Properties of molecules with a larger average size, where Vina stands for Vina Dock Avg., SR for Success Rate.

Methods	Vina	QED	SA	SR	Size
Reference	-7.45	0.48	0.73	25.0%	22.8
DecompDiff	-8.39	0.45	0.61	24.5%	29.4
DecompOpt	-9.01	0.48	0.65	52.5%	32.9
MolCRAFT	-9.25	0.46	0.62	36.6%	29.4
MolJO	-10.53	0.50	0.72	64.2%	30.0

cal use cases including R-group optimization and scaffold hopping, achieved by infilling (details in Appendix D.2).

MolJO captures the complex environment of infilling.

Table 2 shows that our method generates valid connected molecules and captures the complicated chemical environment with better molecular properties than all baselines, showcasing its potential for lead optimization. As for

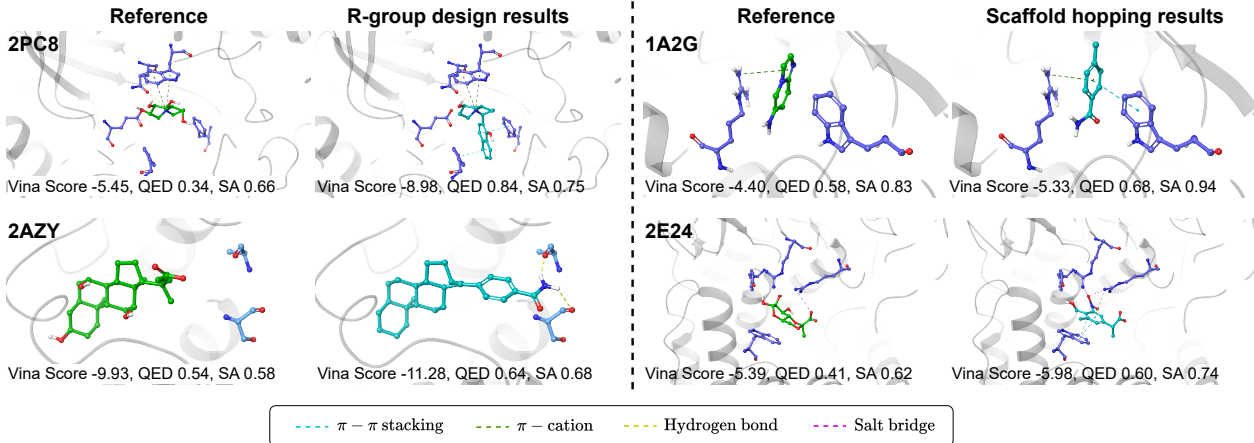


Figure 3. Visualization of the binding modes of the reference molecule (carbons in green) and the optimized molecule (in cyan) within the protein pocket (PDB ID: 2PC8, 2AZY, 1A2G, 2E24). The molecules and key residues (in blue) are shown in stick, while the protein’s main chain is drawn in cartoon (in gray). Dashed lines of various colors indicate different types of non-bonding interactions. **Left:** R-group optimization results. **Right:** scaffold hopping results.

Table 4. Performances of no correction (*Vanilla*), SDE and backward correction strategy (*B.C.*) without and with gradient guidance. Positive numbers in green show the relative improvement, while non-positive numbers in black indicate no performance gain.

Grad	Sampling	Vina Score (↓)		Vina Min (↓)		Vina Dock (↓)		QED (↑) Avg.	SA (↑) Avg.
		Avg.	Med.	Avg.	Med.	Avg.	Med.		
✗	Vanilla	-5.23	-5.81	-6.30	-6.17	-7.37	-7.31	0.46	0.62
	SDE	-6.62	-7.08	-7.31	-7.24	-8.22	-8.32	0.51	0.65
	B.C.	-6.50	-7.00	-7.03	-7.14	-7.95	-7.87	0.49	0.69
✓	Vanilla	-5.47 (+4.6%)	-5.89 (+1.4%)	-6.29 (-0.2%)	-6.31 (+2.3%)	-7.49 (+2.2%)	-7.46 (+2.1%)	0.46 (+0.0%)	0.62 (+0.0%)
	SDE	-7.11 (+7.4%)	-7.53 (+6.3%)	-7.76 (+6.1%)	-7.73 (+6.8%)	-8.39 (+2.1%)	-8.66 (+4.1%)	0.50 (-1.9%)	0.68 (+4.6%)
	B.C.	-7.52 (+15.7%)	-8.06 (+15.1%)	-8.34 (+18.6%)	-8.40 (+17.6%)	-9.11 (+14.6%)	-9.25 (+17.5%)	0.56 (+14.3%)	0.77 (+11.6%)

diffusion baselines, they generate fewer valid connected molecules especially in the challenging case with scaffold hopping, with diffusion baselines lower than 70% validity, and proves to be less effective in proposing feasible candidates, with Success Rate < 20%.

Optimized molecules form more key interactions for binding. The visualization for constrained optimization is shown in Fig. 3. It can be seen that the optimized molecules establish more key interactions with the protein pockets, thus binding more tightly to the active sites. For example, the optimized molecule for 2PC8 retains the key interaction formed by its scaffold, with R-group grown deeper inside the pocket, forming another two $\pi-\pi$ stackings.

5.4. Ablation Studies

We conduct ablation studies to thoroughly validate our design. More details are left to Appendix F.2. For all the 100 test proteins, we sample 10 molecules each.

Joint guidance is consistently better than single-modality guidance. To validate our choice of joint guidance over

different modalities, we ablate the gradient for coordinates or types. As shown in Table 11, utilizing gradients to guide both data modalities is consistently better than applying single-modality gradient only. For affinities, optimizing coordinates is effective in improving the spatial interactions, while for drug-like properties, guidance over atom types plays a crucial role. This underscores the significance of deriving appropriate guidance form jointly, and again supports our finding that a single coordinate guidance as in TAGMol is insufficient and yields suboptimal results.

Backward correction boosts both the unguided sampling and the effect of guidance. We denote sampling θ_i according to Eq. 10 *Vanilla* for point estimate of $y \sim ps$ in Eq. 1, advanced *SDE* proposed by Xue et al. (2024) with classifier guidance, and for *B.C.* we set $k = 130$ as backward correction steps. Table 4 shows that our method of correcting the past yields better results with guidance. Note that for vanilla case, the gradient guidance does not work as much probably due to the suboptimal history, and SDE-based classifier guidance may have suffered from discretization errors, while correcting a sufficient number of past steps shows consistent boosts.

6. Conclusion

We present MolJO, the joint gradient-based SE(3)-equivariant framework within Bayesian Flow Networks to solve the structure-based molecule optimization problems, which only requires differentiable energy functions instead of expensive oracle simulations. The general framework further equips gradient-based optimization method with backward correction strategy, offering a flexible trade-off between exploration and exploitation. Experiments show that MolJO is able to improve the binding affinity of molecules by establishing more key interactions and enhance drug-likeness and synthesizability, achieving state-of-the-art performance on CrossDocked2020 (Success Rate 51.3%, Vina Dock -9.05 and SA 0.78), together with 4 \times improvement compared to gradient-based counterpart and 2 \times “Me-Better” Ratio as other 3D baselines.

Impact Statement

This work is aimed at facilitating structure-based molecule optimziation (SBMO) for drug discovery pipeline. The positive societal impacts include effective design of viable drug candidates. While there is a minimal risk of misuse for generating harmful substances, such risks are mitigated by the need for significant laboratory resources and ethical conduct.

Acknowledgments

This work is supported by the Natural Science Foundation of China (Grant No. 62376133) and sponsored by Beijing Nova Program (20240484682) and the Wuxi Research Institute of Applied Technologies, Tsinghua University (20242001120).

References

- Bao, F., Zhao, M., Hao, Z., Li, P., Li, C., and Zhu, J. Equivariant energy-guided sde for inverse molecular design. In *The eleventh international conference on learning representations*, 2022.
- Bengio, E., Jain, M., Korablyov, M., Precup, D., and Bengio, Y. Flow network based generative models for non-iterative diverse candidate generation. *Advances in Neural Information Processing Systems*, 34:27381–27394, 2021.
- Bilodeau, C., Jin, W., Jaakkola, T., Barzilay, R., and Jensen, K. F. Generative models for molecular discovery: Recent advances and challenges. *Wiley Interdisciplinary Reviews: Computational Molecular Science*, 12(5):e1608, 2022.
- Bjerrum, E. J. and Threlfall, R. Molecular generation with recurrent neural networks (rnns). *arXiv preprint arXiv:1705.04612*, 2017.
- Cheng, X., Zhou, X., Yang, Y., Bao, Y., and Gu, Q. Decomposed direct preference optimization for structure-based drug design, 2025. URL <https://openreview.net/forum?id=blSYKTWurU>.
- Dhariwal, P. and Nichol, A. Diffusion models beat gans on image synthesis. *Advances in neural information processing systems*, 34:8780–8794, 2021.
- Dorna, V., Subhalingam, D., Kolluru, K., Tuli, S., Singh, M., Singal, S., Krishnan, N. M. A., and Ranu, S. Tagmol: Target-aware gradient-guided molecule generation. *arXiv preprint arXiv:2406.01650*, 2024.
- Du, Y., Jamasb, A. R., Guo, J., Fu, T., Harris, C., Wang, Y., Duan, C., Liò, P., Schwaller, P., and Blundell, T. L. Machine learning-aided generative molecular design. *Nature Machine Intelligence*, pp. 1–16, 2024.
- Eberhardt, J., Santos-Martins, D., Tillack, A. F., and Forli, S. Autodock vina 1.2. 0: New docking methods, expanded force field, and python bindings. *Journal of chemical information and modeling*, 61(8):3891–3898, 2021.
- Epstein, D., Jabri, A., Poole, B., Efros, A., and Holynski, A. Diffusion self-guidance for controllable image generation. *Advances in Neural Information Processing Systems*, 36: 16222–16239, 2023.
- Francoeur, P. G., Masuda, T., Sunseri, J., Jia, A., Iovanisci, R. B., Snyder, I., and Koes, D. R. Three-dimensional convolutional neural networks and a cross-docked data set for structure-based drug design. *Journal of chemical information and modeling*, 60(9):4200–4215, 2020.
- Fu, T., Gao, W., Coley, C., and Sun, J. Reinforced genetic algorithm for structure-based drug design. *Advances in Neural Information Processing Systems*, 35:12325–12338, 2022.
- Gómez-Bombarelli, R., Wei, J. N., Duvenaud, D., Hernández-Lobato, J. M., Sánchez-Lengeling, B., Sheberla, D., Aguilera-Iparraguirre, J., Hirzel, T. D., Adams, R. P., and Aspuru-Guzik, A. Automatic chemical design using a data-driven continuous representation of molecules. *ACS central science*, 4(2):268–276, 2018.
- Graves, A., Srivastava, R. K., Atkinson, T., and Gomez, F. Bayesian flow networks. *arXiv preprint arXiv:2308.07037*, 2023.
- Guan, J., Qian, W. W., Peng, X., Su, Y., Peng, J., and Ma, J. 3d equivariant diffusion for target-aware molecule generation and affinity prediction. In *The Eleventh International Conference on Learning Representations*, 2022.

- Guan, J., Zhou, X., Yang, Y., Bao, Y., Peng, J., Ma, J., Liu, Q., Wang, L., and Gu, Q. DecomDiff: Diffusion models with decomposed priors for structure-based drug design. In Krause, A., Brunskill, E., Cho, K., Engelhardt, B., Sabato, S., and Scarlett, J. (eds.), *Proceedings of the 40th International Conference on Machine Learning*, volume 202 of *Proceedings of Machine Learning Research*, pp. 11827–11846. PMLR, 23–29 Jul 2023. URL <https://proceedings.mlr.press/v202/guan23a.html>.
- Halgren, T. A., Murphy, R. B., Friesner, R. A., Beard, H. S., Frye, L. L., Pollard, W. T., and Banks, J. L. Glide: a new approach for rapid, accurate docking and scoring. 2. enrichment factors in database screening. *Journal of medicinal chemistry*, 47(7):1750–1759, 2004.
- Han, X., Shan, C., Shen, Y., Xu, C., Yang, H., Li, X., and Li, D. Training-free multi-objective diffusion model for 3d molecule generation. In *The Twelfth International Conference on Learning Representations*, 2023.
- Harris, C., Didi, K., Jamasb, A. R., Joshi, C. K., Mathis, S. V., Lio, P., and Blundell, T. Benchmarking generated poses: How rational is structure-based drug design with generative models? *arXiv preprint arXiv:2308.07413*, 2023.
- Hinton, G. E. Training products of experts by minimizing contrastive divergence. *Neural Computation*, 14(8):1771–1800, 2002. doi: 10.1162/089976602760128018.
- Huang, Z., Yang, L., Zhou, X., Zhang, Z., Zhang, W., Zheng, X., Chen, J., Wang, Y., Bin, C., and Yang, W. Protein-ligand interaction prior for binding-aware 3d molecule diffusion models. In *The Twelfth International Conference on Learning Representations*, 2024.
- Hughes, J. P., Rees, S., Kalindjian, S. B., and Philpott, K. L. Principles of early drug discovery. *British journal of pharmacology*, 162(6):1239–1249, 2011.
- Isert, C., Atz, K., and Schneider, G. Structure-based drug design with geometric deep learning. *Current Opinion in Structural Biology*, 79:102548, April 2023. ISSN 0959440X. doi: 10.1016/j.sbi.2023.102548. URL <https://linkinghub.elsevier.com/retrieve/pii/S0959440X23000222>.
- Jin, W., Barzilay, R., and Jaakkola, T. Junction tree variational autoencoder for molecular graph generation. In *International conference on machine learning*, pp. 2323–2332. PMLR, 2018.
- Kong, L., Cui, J., Sun, H., Zhuang, Y., Prakash, B. A., and Zhang, C. Autoregressive diffusion model for graph generation. In Krause, A., Brunskill, E., Cho, K., Engelhardt, B., Sabato, S., and Scarlett, J. (eds.), *Proceedings of the 40th International Conference on Machine Learning*, volume 202 of *Proceedings of Machine Learning Research*, pp. 17391–17408. PMLR, 23–29 Jul 2023. URL <https://proceedings.mlr.press/v202/kong23b.html>.
- Kong, L., Du, Y., Mu, W., Neklyudov, K., De Bortol, V., Wang, H., Wu, D., Ferber, A., Ma, Y.-A., Gomes, C. P., et al. Diffusion models as constrained samplers for optimization with unknown constraints. *arXiv preprint arXiv:2402.18012*, 2024.
- Lin, H., Huang, Y., Liu, M., Li, X., Ji, S., and Li, S. Z. Diffbp: Generative diffusion of 3d molecules for target protein binding, 2022.
- Lin, H., Huang, Y., Zhang, O., Liu, Y., Wu, L., Li, S., Chen, Z., and Li, S. Z. Functional-group-based diffusion for pocket-specific molecule generation and elaboration. In Oh, A., Naumann, T., Globerson, A., Saenko, K., Hardt, M., and Levine, S. (eds.), *Advances in Neural Information Processing Systems*, volume 36, pp. 34603–34626. Curran Associates, Inc., 2023. URL <https://arxiv.org/abs/2306.13769>.
- Lin, H., Huang, Y., Zhang, O., Wu, L., Li, S., Chen, Z., and Li, S. Z. Functional-group-based diffusion for pocket-specific molecule generation and elaboration, 2024.
- Lin, H., Zhao, G., Zhang, O., Huang, Y., Wu, L., Tan, C., Liu, Z., Gao, Z., and Li, S. Z. CBGBench: Fill in the blank of protein-molecule complex binding graph. In *The Thirteenth International Conference on Learning Representations*, 2025. URL <https://openreview.net/forum?id=mOpNrrV2zH>.
- Lipinski, C. A., Lombardo, F., Dominy, B. W., and Feeney, P. J. Experimental and computational approaches to estimate solubility and permeability in drug discovery and development settings. *Advanced drug delivery reviews*, 23(1-3):3–25, 1997.
- Liu, M., Luo, Y., Uchino, K., Maruhashi, K., and Ji, S. Generating 3d molecules for target protein binding. In *International Conference on Machine Learning*, 2022.
- Luo, S., Guan, J., Ma, J., and Peng, J. A 3D Generative Model for Structure-Based Drug Design. *Advances in Neural Information Processing Systems*, 34: 6229–6239, 2021. URL <http://arxiv.org/abs/2203.10446>.
- Nigam, A., Friederich, P., Krenn, M., and Aspuru-Guzik, A. Augmenting genetic algorithms with deep neural networks for exploring the chemical space. In *International Conference on Learning Representations*,

2020. URL <https://openreview.net/forum?id=H1lmyRNFvr>.
- Olivecrona, M., Blaschke, T., Engkvist, O., and Chen, H. Molecular de-novo design through deep reinforcement learning. *Journal of cheminformatics*, 9(1):1–14, 2017.
- Peng, X., Luo, S., Guan, J., Xie, Q., Peng, J., and Ma, J. Pocket2Mol: Efficient molecular sampling based on 3D protein pockets. In Chaudhuri, K., Jegelka, S., Song, L., Szepesvari, C., Niu, G., and Sabato, S. (eds.), *Proceedings of the 39th International Conference on Machine Learning*, volume 162 of *Proceedings of Machine Learning Research*, pp. 17644–17655. PMLR, 17–23 Jul 2022. URL <https://proceedings.mlr.press/v162/peng22b.html>.
- Pinheiro, P. O., Jamasb, A., Mahmood, O., Sresht, V., and Saremi, S. Structure-based drug design by denoising voxel grids. In *ICML*, 2024.
- Polykovskiy, D., Zhebrak, A., Sanchez-Lengeling, B., Golovanov, S., Tatanov, O., Belyaev, S., Kurbanov, R., Artamonov, A., Aladinskiy, V., Veselov, M., et al. Molecular sets (moses): a benchmarking platform for molecular generation models. *Frontiers in pharmacology*, 11:565644, 2020.
- Powers, A. S., Yu, H. H., Suriana, P. A., and Dror, R. O. Fragment-based ligand generation guided by geometric deep learning on protein-ligand structures. In *ICLR2022 Machine Learning for Drug Discovery*, 2022. URL <https://openreview.net/forum?id=192L9cr-8HU>.
- Qu, Y., Qiu, K., Song, Y., Gong, J., Han, J., Zheng, M., Zhou, H., and Ma, W.-Y. MolCRAFT: Structure-based drug design in continuous parameter space. In *Forty-first International Conference on Machine Learning*, 2024. URL <https://openreview.net/forum?id=KaAQu5rNU1>.
- Schneuing, A., Du, Y., Harris, C., Jamasb, A., Igashov, I., Du, W., Blundell, T., Lió, P., Gomes, C., Welling, M., Bronstein, M., and Correia, B. Structure-based Drug Design with Equivariant Diffusion Models, October 2022. URL <http://arxiv.org/abs/2210.13695>. arXiv:2210.13695 [cs, q-bio].
- Song, Y., Gong, J., Qu, Y., Zhou, H., Zheng, M., Liu, J., and Ma, W.-Y. Unified generative modeling of 3d molecules via bayesian flow networks. *arXiv preprint arXiv:2403.15441*, 2024.
- Spiegel, J. O. and Durrant, J. D. Autogrow4: an open-source genetic algorithm for de novo drug design and lead optimization. *Journal of cheminformatics*, 12:1–16, 2020.
- Sun, F., Zhan, Z., Guo, H., Zhang, M., and Tang, J. Graphvf: Controllable protein-specific 3d molecule generation with variational flow, 2023. URL <https://arxiv.org/abs/2304.12825>.
- Vignac, C., Krawczuk, I., Siraudin, A., Wang, B., Cevher, V., and Frossard, P. Digress: Discrete denoising diffusion for graph generation. In *The Eleventh International Conference on Learning Representations*, 2023. URL <https://openreview.net/forum?id=UaAD-Nu86WX>.
- Wu, H., Song, Y., Gong, J., Cao, Z., Ouyang, Y., Zhang, J., Zhou, H., Ma, W.-Y., and Liu, J. A periodic bayesian flow for material generation. In *The Thirteenth International Conference on Learning Representations*, 2025. URL <https://openreview.net/forum?id=Lz0XW99tE0>.
- Xie, Y., Shi, C., Zhou, H., Yang, Y., Zhang, W., Yu, Y., and Li, L. {MARS}: Markov molecular sampling for multi-objective drug discovery. In *International Conference on Learning Representations*, 2021. URL <https://openreview.net/forum?id=kHSu4ebxFXY>.
- Xue, K., Zhou, Y., Nie, S., Min, X., Zhang, X., ZHOU, J., and Li, C. Unifying bayesian flow networks and diffusion models through stochastic differential equations. In *Forty-first International Conference on Machine Learning*, 2024. URL <https://openreview.net/forum?id=1jHiq640yl>.
- Zhang, Z., Min, Y., Zheng, S., and Liu, Q. Molecule Generation For Target Protein Binding with Structural Motifs. 2023.
- Zhou, X., Cheng, X., Yang, Y., Bao, Y., Wang, L., and Gu, Q. Decompopt: Controllable and decomposed diffusion models for structure-based molecular optimization. *arXiv preprint arXiv:2403.13829*, 2024a.
- Zhou, X., Wang, L., and Zhou, Y. Stabilizing policy gradients for stochastic differential equations via consistency with perturbation process. In *Forty-first International Conference on Machine Learning*, 2024b. URL <https://openreview.net/forum?id=ytz2naZoDB>.

A. Overview of Bayesian Flow Networks

In this section, we provide further explanation of Bayesian Flow Networks (BFNs) that are designed to model the generation of data through a process of message exchange between a “sender” and a “receiver” (Graves et al., 2023). The fundamental elements include the sender distribution for the sender, and input distribution, output distribution, receiver distribution for the receiver.

This process is framed within the context of Bayesian inference, where the *sender distribution* is a factorized distribution $p_S(\mathbf{y}|\mathbf{m}, \alpha_t)$ that introduces noise to each dimension of the data \mathbf{m} and sends it to the receiver. The receiver observes \mathbf{y} , has access to the noisy channel with accuracy α at timestep t , and compares it with its own *receiver distribution* $p_R(\mathbf{y}|\theta, \mathbf{p}; t)$ based on its current belief of the parameters θ , the timestep and any conditional input such as protein pocket \mathbf{p} .

The generative process for the receiver begins with a prior distribution (referred to as *input distribution* $p_I(\mathbf{m}|\theta) = \prod_{d=1}^N p_I(m^{(d)}|\theta^{(d)})$ that is also factorized for N -dimensional data) that defines its initial belief about the data. For continuous data, the prior can be chosen as a Gaussian (Song et al., 2024; Qu et al., 2024), or another distribution such as von Mises distribution (Wu et al., 2025), while for discrete data, the prior is modeled as a uniform categorical distribution. Then, the receiver uses its belief θ with the help of a neural network to model the inter-dependency among dimensions and compute the *output distribution* $p_O(\hat{\mathbf{m}}|\theta, \mathbf{p}; t)$, which represents its estimate of the possible reconstructions of the original data \mathbf{m} , and is used to construct the receiver distribution (Eq. 2).

The Bayesian update function in Eq. 1 defines how the prior belief θ_0 is updated to the conjugate posterior θ_t . Ideally, the update requires aggregating all possible noisy latents \mathbf{y} from the sender distribution p_S . However, during the actual generative process, only the receiver distribution p_R is available, which leaves an exposure bias, and different approximations determine different forms of mapping $\theta = f(\mathbf{y})$ to the posterior, showcasing the flexibility in the design space of BFN.

Through the iterative communication between sender and receiver, the receiver progressively updates its belief of the underlying parameters, and training is achieved by minimizing the divergence between the sender and receiver distributions (Eq. 3). This is analogous to the way Bayesian inference works in parameter estimation: as more noisy data \mathbf{y} is observed, the receiver’s posterior belief about the data \mathbf{m} becomes increasingly accurate, which implies the reconstruction would be made easier. It is shown that BFN for Gaussian priors can be sampled from the view of SDE (Xue et al., 2024), but this type of sampling displays distinct behaviors empirically, possibly due to discretization errors.

B. Sender Distribution for Discrete Data

The continuous parameter θ^v for discrete types v is updated by observed noisy \mathbf{y}^v . Here we briefly introduce how to configure the sender so that \mathbf{y}^v follows a Gaussian as well. For detailed derivation, we refer the readers to Graves et al. (2023).

While true discrete data can be viewed as a sharp one-hot distribution, it can be further relaxed by a factor $\omega \in [0, 1]$ into a Categorical distribution defined by the probability $p(k^{(d)}|\mathbf{v}^{(d)}; \omega) = \frac{1-\omega}{K} + \omega\delta_{k^{(d)}\mathbf{v}^{(d)}}$ for k from 1 to K along the d -th dimension, where δ is the Kronecker delta function.

Instead of focusing on the density or sampling from it once, note that the counts c of observing each class in m independent draws follow a multinomial distribution, namely $c \sim \text{Multi}(m, p)$. Dropping the superscripts, Graves et al. (2023) derives the following conclusions:

Proposition B.1. *When the number of experiments m is large enough, the frequency approximates its density for class indexed at k , i.e. $\lim_{m \rightarrow \infty} \frac{c_k}{m} = p(k|\mathbf{v}; \omega)$, following the law of large numbers. Furthermore, by the central limit theorem, it follows that $\frac{c - mp}{\sqrt{mp(1-p)}} \sim \mathcal{N}(0, \mathbf{I})$ when $m \rightarrow \infty$.*

Proposition B.2. *Denoting $y_k = (c_k - \frac{m}{K}) \ln \xi$ with $\xi = 1 + \frac{\omega K}{1-\omega}$, and $p_S(y_k|\mathbf{v}; \alpha) = \lim_{\omega \rightarrow 0} p(y_k|\mathbf{v}; \omega)$ with $\alpha = m\omega^2$, it holds from the change of variables that $p_S(y_k|\mathbf{v}; \alpha) = \mathcal{N}(\alpha(K\delta_{k\mathbf{v}} - 1), \alpha K)$.*

Thus, it naturally follows that such noisy $\mathbf{y}^v \sim \mathcal{N}(\mathbf{y}^v|\alpha(K\mathbf{e}_v - \mathbf{1}), \alpha K\mathbf{I})$.

C. Proofs

C.1. Proof of Guided Bayesian Update Distribution

Lemma. If a random vector \mathbf{X} has probability density $f(\mathbf{x}) \propto \mathcal{N}(\mathbf{x}|\boldsymbol{\theta}^x, \Sigma) e^{\mathbf{c}^T \mathbf{x}}$, where \mathbf{c} is a constant vector with the same dimension as \mathbf{X} , then $\mathbf{X} \sim \mathcal{N}(\boldsymbol{\theta}^x + \Sigma \mathbf{c}, \Sigma)$.

Proof. We obtain the proof by completing the square as shown below.

$$\begin{aligned}\log f(\mathbf{x}) &= C - \frac{1}{2}(\mathbf{x} - \boldsymbol{\theta}^x)^T \Sigma^{-1}(\mathbf{x} - \boldsymbol{\theta}^x) + \mathbf{c}^T \mathbf{x} \\ &= C' - \frac{1}{2}(\mathbf{x} - \boldsymbol{\theta}^x - \Sigma \mathbf{c})^T \Sigma^{-1}(\mathbf{x} - \boldsymbol{\theta}^x - \Sigma \mathbf{c})\end{aligned}\quad (15)$$

where C and C' are constant scalars. \square

Proposition (4.1). Assuming $\boldsymbol{\theta}_i^x \sim \mathcal{N}(\boldsymbol{\theta}_\phi^x, \sigma)$ and $\mathbf{y}_i^v \sim \mathcal{N}(\mathbf{y}_\phi, \sigma)$ by definition of the generative process of BFN, we can approximately sample $\boldsymbol{\theta}_i^x, \mathbf{y}_i^v$ from the guided transition kernel $\pi(\boldsymbol{\theta}_i|\boldsymbol{\theta}_{i-1})$ according to Eq. 4 and 5.

Proof. Under the definition of π , with the parameters $\boldsymbol{\theta}_i = [\boldsymbol{\theta}_i^x, \boldsymbol{\theta}_i^v]$ referred to as $[\boldsymbol{\theta}_i^x, \boldsymbol{\theta}_i^v(\mathbf{y}_i^v)]$ and a slight abuse of notation, we have

$$\pi(\boldsymbol{\theta}_i^x, \mathbf{y}_i^v|\boldsymbol{\theta}_{i-1}) \propto p_\phi(\boldsymbol{\theta}_i^x, \mathbf{y}_i^v|\boldsymbol{\theta}_{i-1}) p_E(\boldsymbol{\theta}_i^x, \mathbf{y}_i^v) \quad (16)$$

where some parentheses and protein pocket condition \mathbf{p} have been omitted for brevity.

Eq. 13 and 14 guarantee that $\boldsymbol{\theta}_i^x \sim \mathcal{N}(\boldsymbol{\theta}_\phi^x, \sigma^x)$, $\mathbf{y}_i^v \sim \mathcal{N}(\mathbf{y}_\phi, \sigma^v)$. Plugging $p_E(\boldsymbol{\theta}_i^x, \mathbf{y}_i^v) \propto e^{-E(\boldsymbol{\theta}_i^x, \mathbf{y}_i^v, t_i)}$ into Eq. 16, we get

$$\pi(\boldsymbol{\theta}_i^x, \mathbf{y}_i^v|\boldsymbol{\theta}_{i-1}) \propto \mathcal{N}(\boldsymbol{\theta}_\phi^x, \sigma^x) \mathcal{N}(\mathbf{y}_i^v|\mathbf{y}_\phi, \sigma^v) e^{-E(\boldsymbol{\theta}_i^x, \mathbf{y}_i^v, t_i)} \quad (17)$$

With t_i fixed, perform a first-order Taylor expansion to $E(\boldsymbol{\theta}^x, \mathbf{y}^v, t_i)$ at $(\boldsymbol{\theta}_{i-1}^x, \mathbf{y}_{i-1}^v)$:

$$E(\boldsymbol{\theta}_i^x, \mathbf{y}_i^v, t_i) \approx E(\boldsymbol{\theta}_{i-1}^x, \mathbf{y}_{i-1}^v, t_i) - \mathbf{g}_{\boldsymbol{\theta}^x}^T(\boldsymbol{\theta}_i^x - \boldsymbol{\theta}_{i-1}^x) - \mathbf{g}_{\mathbf{y}}^T(\mathbf{y}_i^v - \mathbf{y}_{i-1}^v) \quad (18)$$

where gradient $\mathbf{g}_{\boldsymbol{\theta}^x} = -\nabla_{\boldsymbol{\theta}^x} E(\boldsymbol{\theta}, t_i)|_{\boldsymbol{\theta}=\boldsymbol{\theta}_{i-1}}$, $\mathbf{g}_{\mathbf{y}} = -\nabla_{\mathbf{y}} E(\boldsymbol{\theta}, t_i)|_{\boldsymbol{\theta}=\boldsymbol{\theta}_{i-1}}$. Substitute it into Eq. 17:

$$\pi(\boldsymbol{\theta}_i^x, \mathbf{y}_i^v|\boldsymbol{\theta}_{i-1}) \stackrel{\text{apx}}{\propto} \mathcal{N}(\boldsymbol{\theta}_i^x|\boldsymbol{\theta}_\phi^x, \sigma^x) \mathcal{N}(\mathbf{y}_i^v|\mathbf{y}_\phi, \sigma^v) e^{\mathbf{g}_{\boldsymbol{\theta}^x}^T \boldsymbol{\theta}_i^x + \mathbf{g}_{\mathbf{y}}^T \mathbf{y}_i^v} \quad (19)$$

Eq. 19, together with the lemma above, leads to Proposition 4.1. \square

C.2. Proof of Equivariance

Proposition (4.4). The guided sampling process preserves SE(3)-equivariance when Φ is SE(3)-equivariant, if the energy function $E(\boldsymbol{\theta}, \mathbf{p}, t)$ is also parameterized with an SE(3)-equivariant neural network, and the complex is shifted to the space where the protein's Center of Mass (CoM) is zero.

Proof. Following Schneuing et al. (2022), once the complex is moved so that the pocket is centered at the origin (*i.e.* zero CoM), translation equivariance becomes irrelevant and only O(3)-equivariance needs to be satisfied.

For any orthogonal matrix $\mathbf{R} \in \mathbb{R}^{3 \times 3}$ such that $\mathbf{R}^T \mathbf{R} = \mathbf{I}$, it is easy to see that the prior $\boldsymbol{\theta}_0^x = \mathbf{0}$ is O(3)-invariant. Given that $\hat{\mathbf{x}} \sim p_O(\hat{\mathbf{x}} | \Phi(\boldsymbol{\theta}, \mathbf{p}, t))$ and the equivariance of Φ , it suffices to prove the invariant likelihood for the transition kernel.

Given the parameterization of the pretrained energy function $E(\boldsymbol{\theta}, \mathbf{p}, t)$ is SE(3)-equivariant, then the gradient $\mathbf{g}_{\boldsymbol{\theta}^x}(\boldsymbol{\theta}) = -\nabla_{\boldsymbol{\theta}^x} E(\boldsymbol{\theta}, \mathbf{p}, t_i)$ is also equivariant according to Bao et al. (2022).

Without loss of generality, we consider the guided transition density for $i \leq k$, which simplifies to

$$\begin{aligned}\pi(\boldsymbol{\theta}_i^x | \boldsymbol{\theta}_{i-1}^x, \mathbf{y}_{i-1}^v, \mathbf{p}) \\ = \mathcal{N}(\boldsymbol{\theta}_i^x | \gamma_i \Phi(\boldsymbol{\theta}_{i-1}^x, \mathbf{y}_{i-1}^v, \mathbf{p}) + \gamma_i(1 - \gamma_i) \mathbf{g}_{\boldsymbol{\theta}^x}(\boldsymbol{\theta}_{i-1}^x, \mathbf{y}_{i-1}^v, \mathbf{p}, t_{i-1}), \gamma_i(1 - \gamma_i) \mathbf{I})\end{aligned}$$

where $\gamma_i \stackrel{\text{def}}{=} \frac{\beta(t_i)}{1+\beta(t_i)}$.

Then we can prove that it is O(3)-invariant:

$$\begin{aligned}
 & \pi(\mathbf{R}\boldsymbol{\theta}_i^x \mid \mathbf{R}\boldsymbol{\theta}_{i-1}^x, \mathbf{y}_{i-1}^v, \mathbf{Rp}) \\
 &= \mathcal{N}(\mathbf{R}\boldsymbol{\theta}_i^x \mid \gamma_i \Phi(\mathbf{R}\boldsymbol{\theta}_{i-1}^x, \mathbf{y}_{i-1}^v, \mathbf{Rp}) + \gamma_i(1 - \gamma_i) \mathbf{g}_{\boldsymbol{\theta}^x}(\mathbf{R}\boldsymbol{\theta}_{i-1}^x, \mathbf{y}_{i-1}^v, \mathbf{Rp}, t_{i-1}), \gamma_i(1 - \gamma_i) \mathbf{I}) \\
 &= \mathcal{N}(\mathbf{R}\boldsymbol{\theta}_i^x \mid \gamma_i \Phi(\mathbf{R}\boldsymbol{\theta}_{i-1}^x, \mathbf{y}_{i-1}^v, \mathbf{Rp}) + \gamma_i(1 - \gamma_i) \mathbf{R}\mathbf{g}_{\boldsymbol{\theta}^x}(\boldsymbol{\theta}_{i-1}^x, \mathbf{y}_{i-1}^v, \mathbf{p}, t_{i-1}), \gamma_i(1 - \gamma_i) \mathbf{I}) \\
 &\quad \text{(equivariance of } \mathbf{g}_{\boldsymbol{\theta}^x} \text{)} \\
 &= \mathcal{N}(\mathbf{R}\boldsymbol{\theta}_i^x \mid \gamma_i \mathbf{R}\Phi(\boldsymbol{\theta}_{i-1}^x, \mathbf{y}_{i-1}^v, \mathbf{p}) + \gamma_i(1 - \gamma_i) \mathbf{R}\mathbf{g}_{\boldsymbol{\theta}^x}(\boldsymbol{\theta}_{i-1}^x, \mathbf{y}_{i-1}^v, \mathbf{p}, t_{i-1}), \gamma_i(1 - \gamma_i) \mathbf{I}) \\
 &\quad \text{(equivariance of } \Phi \text{)} \\
 &= \mathcal{N}(\boldsymbol{\theta}_i^x \mid \gamma_i \Phi(\boldsymbol{\theta}_{i-1}^x, \mathbf{y}_{i-1}^v, \mathbf{p}) + \gamma_i(1 - \gamma_i) \mathbf{g}_{\boldsymbol{\theta}^x}(\boldsymbol{\theta}_{i-1}^x, \mathbf{y}_{i-1}^v, \mathbf{p}, t_{i-1}), \gamma_i(1 - \gamma_i) \mathbf{I}) \\
 &\quad \text{(equivariance of isotropic Gaussian)} \\
 &= \pi(\boldsymbol{\theta}_i^x \mid \boldsymbol{\theta}_{i-1}^x, \mathbf{y}_{i-1}^v, \mathbf{p})
 \end{aligned}$$

It also applies to cases where $i > k$, as we can recurrently view the starting point of backward corrected history $\boldsymbol{\theta}_{i-k}^x$ as the new O(3)-invariant prior $\boldsymbol{\theta}_0^x$ and iteratively make the above derivation. \square

D. Implementation Details

D.1. Model Details

Backbone. Our BFN backbone follows that of MolCRAFT (Qu et al., 2024), and we conduct optimization during sampling on the pretrained checkpoint without finetuning.

Training Property Regressors. To enable a differentiable oracle function, we additionally train the energy function based on the molecules and their properties (Vina Score, QED, SA) in CrossDocked dataset (Francoeur et al., 2020) by minimizing the squared loss for property c over the data distribution p_{data} :

$$L = \mathbb{E}_{p_{\text{data}}} |E(\boldsymbol{\theta}, \mathbf{p}, t) - c|^2 \quad (20)$$

where the Bayesian posterior is derived by Graves et al. (2023) as:

$$\boldsymbol{\theta}_i^x \sim \mathcal{N}(\boldsymbol{\theta}_i^x \mid \gamma_i \mathbf{x} + \gamma_i(1 - \gamma_i), \gamma_i(1 - \gamma_i) \mathbf{I}) \quad (21)$$

$$\boldsymbol{\theta}_i^v \sim \delta(\boldsymbol{\theta}_i^v - \text{softmax}(\mathbf{y}_i^v)) \quad (22)$$

for $\mathbf{y}_i^v \sim \mathcal{N}(\mathbf{y}^v \mid \beta^v(t_i)(K\mathbf{e}_v - \mathbf{1}), \beta^v(t_i)K\mathbf{I})$, δ is the Dirac delta distribution.

The input parameters to all energy functions belong to the parameter space defined by $\beta_1 = 1.5$ for atom types, $\sigma_1 = 0.03$ for atom coordinates, $n = 1000$ discrete steps. The energy network is parameterized with the same model architecture as TargetDiff (Guan et al., 2022), *i.e.* kNN graphs with $k = 32$, $N = 9$ layers with $d = 128$ hidden dimension, 16-headed attention, and the same featurization, *i.e.* protein atoms (H, C, N, O, S, Se) and ligand atoms (C, N, O, F, P, S, Cl). For training, the Adam optimizer is adopted with learning rate 0.0005, batch size is set to 8. The training takes less than 8 hours on a single RTX 3090 and converges within 5 epochs.

Sampling. To sample via guided Bayesian flow, we set the sample steps to 200, and the guidance scale to 50. For the combination of different objectives, we simply take an average of different gradients.

D.2. Task Details

R-group optimization. Lead optimization cases involve retaining the scaffold while redesigning the remaining R-groups, usually when the scaffold forms desirable interactions with the protein and anchors the binding mode, and the remaining parts need further modifications to secure this pattern and enhance binding affinity. Following Polykovskiy et al. (2020), we employ RDKit for fragmentation and atom annotation with R-group or Bemis-Murcko scaffold.

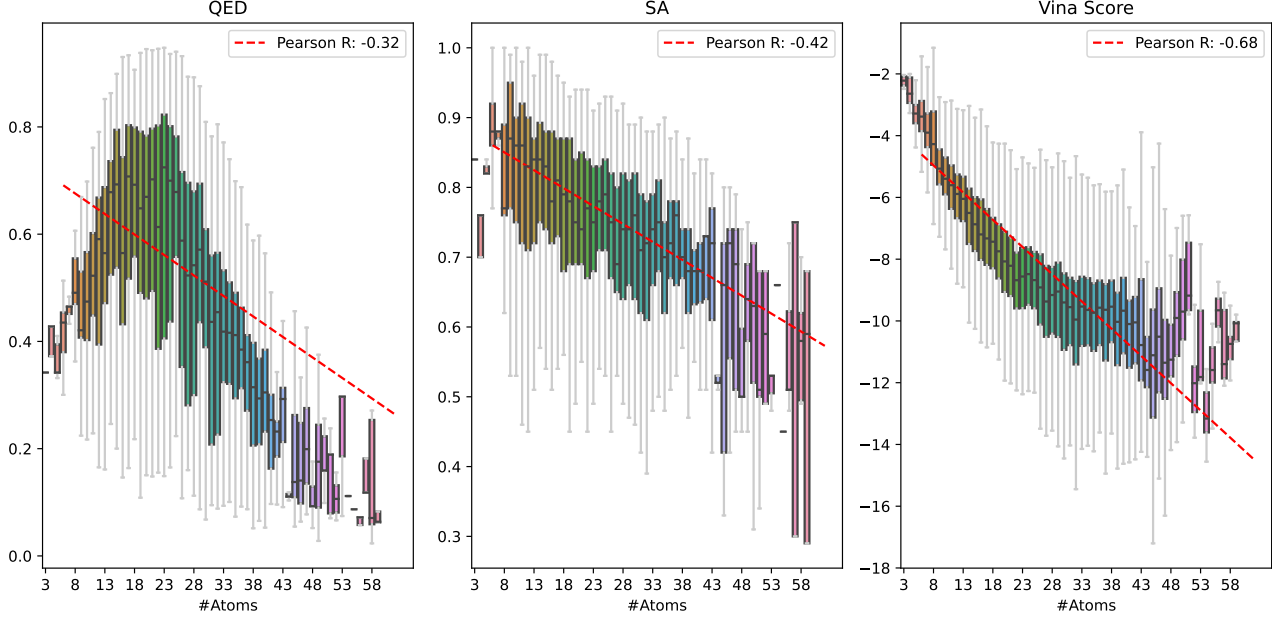


Figure 4. Distribution of molecular properties (QED, SA, Vina Score) over the number of atoms for CrossDocked2020. For each size, the mean and error bars are shown in the boxplot.

Table 5. Molecular properties under different sizes, where *Ref Size* denotes 23 atoms on average, and *Large Size* around 30 atoms. Top 1 results are highlighted with **bold text** for each size category.

Methods		Vina Score (\downarrow)		Vina Min (\downarrow)		Vina Dock (\downarrow)		QED (\uparrow)		SA (\uparrow)		Div (\uparrow)		Success Rate (\uparrow)	
		Avg.	Med.	Avg.	Med.	Avg.	Med.	Avg.	Med.	Avg.	Med.	Avg.	Med.	Avg.	Med.
Ref Size	DecompDiff	-5.19	-5.27	-6.03	-6.00	-7.03	-7.16	0.51	0.66	0.73	0.66	14.9%	14.9%	14.9%	14.9%
	DecompOpt	-5.75	-5.97	-6.58	-6.70	-7.63	-8.02	0.56	0.73	0.63	0.63	39.4%	39.4%	39.4%	39.4%
	MolCRAFT	-6.59	-7.04	-7.27	-7.26	-7.92	-8.01	0.50	0.69	0.72	0.72	26.0%	26.0%	26.0%	26.0%
	MolJO	-7.52	-8.02	-8.33	-8.34	-9.05	-9.13	0.56	0.78	0.66	0.78	51.3%	51.3%	51.3%	51.3%
Large Size	DecompDiff	-5.67	-6.04	-7.04	-7.09	-8.39	-8.43	0.45	0.61	0.68	0.61	24.5%	24.5%	24.5%	24.5%
	DecompOpt	-5.87	-6.81	-7.35	-7.72	-8.98	-9.01	0.48	0.65	0.60	0.60	52.5%	52.5%	52.5%	52.5%
	MolCRAFT	-6.61	-8.14	-8.14	-8.42	-9.25	-9.20	0.46	0.62	0.61	0.61	36.6%	36.6%	36.6%	36.6%
	MolJO	-7.93	-9.26	-9.47	-9.73	-10.53	-10.48	0.50	0.72	0.57	0.72	64.2%	64.2%	64.2%	64.2%

Scaffold hopping. Unlike R-group design, scaffold hopping involves redesigning the scaffold for a given molecule while keeping its core functional groups, for example, to overcome the patent protection for a known drug molecule while retaining pharmaceutical activity. This is a technically more challenging task for generative models, because the missing parts they need to fulfill are generally larger than those in R-group design, and the hopping is usually subject to more chemical constraints. We construct scaffold hopping as a dual problem to R-group optimization using Bemis-Murcko scaffolding annotation, although it does not need to be so.

E. Effect of Molecular Size on Properties

The size of molecules is found to have a notable impact on molecular properties, including Vina affinities (Qu et al., 2024). We quantify the relationship and plot the distribution of molecular properties w.r.t. the number of atoms with the Pearson correlation coefficient in Fig. 4. It is not surprising to see a non-negligible correlation between properties and molecular sizes, since the sizes of molecules typically constrain their accessible chemical space. To ensure a fair comparison, we adhere to the molecular space with similar size to the reference. For further comparison among different model variants, we report the molecular properties under different sizes in Table 5. Results show that our method consistently achieves the highest success rate, demonstrating its robust optimization ability even in an Out-of-Distribution (OOD) scenario.

F. Full Optimization Results

Baselines. We provide a detailed description of all baselines here:

- **AR** (Luo et al., 2021) uses MCMC sampling to reconstruct a molecule atom-by-atom given voxel-wise densities.
- **GraphBP** (Liu et al., 2022) is an autoregressive atom-based model that uses normalizing flow and encodes the context to preserve 3D geometric equivariance.
- **Pocket2Mol** (Peng et al., 2022) generates one atom and its bond at a time via an E(3)-equivariant network. It predicts frontier atoms to expand, alleviating the efficiency problem in sampling.
- **FLAG** (Zhang et al., 2023) is a fragment-based model that assembles the generated fragments using predicted coordinates and torsion angles.
- **DiffSBDD** (Schneuing et al., 2022) constructs an equivariant continuous diffusion for full-atom generation given pocket information, and applies Gaussian noise to both continuous atom coordinates and discrete atom types.
- **TargetDiff** (Guan et al., 2022) adopts a continuous-discrete diffusion approach that treats each modality via corresponding diffusion process, achieving better performance than continuous diffusion such as DiffSBDD.
- **DecompDiff** (Guan et al., 2023) decomposes the molecules into contact arms and linking scaffolds, and utilizes such chemical priors in the diffusion process.
- **IPDiff** (Huang et al., 2024) pretrains an affinity predictor, and utilizes this predictor to extract features that augment the conditioning of the diffusion generative process.
- **MolCRAFT** (Qu et al., 2024) employs Bayesian Flow Networks for molecular design with an advanced sampling strategy, showing notable improvement upon diffusion counterparts.
- **AutoGrow4** (Spiegel & Durrant, 2020) is an evolutionary algorithm that uses a genetic algorithm to optimize 1D SMILES with docking simulation. Starting from the initial seed molecule, AutoGrow4 iteratively conducts mutations and crossovers, then makes oracle calls for docking feedback, and retains the top-scoring molecules in the end.
- **RGA** (Fu et al., 2022) is built on top of AutoGrow4, and utilizes a pocket-aware RL-trained policy to suppress its random walking behavior in traversing the molecular space.
- **DecompOpt** (Zhou et al., 2024a) trains a conditional generative model on decomposed fragments and the binding pocket, following the style of DecompDiff. The optimization is done by iteratively resampling in the 3D diffusion latent space given the top K arms ranked by oracle functions as updated fragment condition input.
- **TAGMol** (Dorna et al., 2024) exerts gradient-based property guidance on the pretrained TargetDiff backbone, and the gradient is enabled only in the continuous diffusion process for coordinates.

Metrics. Besides the common evaluation metrics such as binding affinities calculated by Autodock Vina (Eberhardt et al., 2021) and QED, SA calculated by RDKit, we elaborate other metrics as follows:

- **Diversity** measures the diversity of generated molecules for each binding site. Following SBDD convention (Luo et al., 2021), it is based on Tanimoto similarity over Morgan fingerprints, and averaged across 100 test proteins.
- **Connected Ratio** is the ratio of complete molecules overall, *i.e.* with only one connected component.
- **Lipinski** enumerates the Lipinski rule of five (Lipinski et al., 1997) and checks how many are satisfied. These rules are typically seen as an empirical reference that helps to predict whether the molecule is likely to be orally bioavailable.
- **Key Interaction**, *i.e.* key non-covalent interactions formed between molecules and protein binding sites as an in-depth measure for binding modes, including π interactions, hydrogen bonds (donor and acceptor), salt bridges and hydrophobic interactions calculated by Schrödinger Glide (Halgren et al., 2004).
- **Strain Energy** measures the internal energy of generated poses, indicating pose quality (Harris et al., 2023).

- **Steric Clash** calculates the number of clashes between generated ligand and protein surface, where clashing means the distance of ligand and protein atoms is within a certain threshold. This reveals the stability of complex to some extend, yet it does not strictly mean a violation of physical constraints, since the protein is not overly rigid and might also undergo spatial rearrangement upon binding, as noted by [Harris et al. \(2023\)](#).
- **Redocking RMSD** reports the percentage of molecules with an RMSD between generated and Vina redocked poses lying within the range of 2Å, which suggests the binding mode remains consistent after redocking.

F.1. Molecule Optimization

Overall Distributions. We additionally report the property distributions for SA, QED and Vina Score in Fig. 12, 13, 14, respectively, demonstrating the efficacy of our proposed method in optimizing a number of objectives for “me-better” drug candidates. We additionally report in Table 6 the error bars as 95% confidence intervals for our main results (Table 1).

Table 6. Main results with error bars as 95% confidence intervals.

Model	Vina Score (↓)	Vina Min (↓)	Vina Dock (↓)	QED (↑)	SA (↑)
Reference	-6.362 ± 0.615	-6.707 ± 0.491	-7.450 ± 0.456	0.476 ± 0.040	0.728 ± 0.027
AR	-5.754 ± 0.066	-6.180 ± 0.049	-6.746 ± 0.082	0.509 ± 0.004	0.635 ± 0.003
Pocket2Mol	-5.139 ± 0.063	-6.415 ± 0.058	-7.152 ± 0.097	0.573 ± 0.003	0.756 ± 0.002
TargetDiff	-5.466 ± 0.172	-6.643 ± 0.102	-7.802 ± 0.075	0.480 ± 0.004	0.585 ± 0.003
FLAG	45.978 ± 0.778	6.173 ± 0.525	-5.237 ± 0.142	0.609 ± 0.003	0.626 ± 0.002
DecompDiff	-5.190 ± 0.060	-6.035 ± 0.048	-7.033 ± 0.073	0.505 ± 0.004	0.661 ± 0.003
IPDiff	-6.417 ± 0.141	-7.448 ± 0.088	-8.572 ± 0.072	0.519 ± 0.004	0.595 ± 0.003
MolCRAFT	-6.587 ± 0.122	-7.265 ± 0.070	-7.924 ± 0.097	0.504 ± 0.004	0.686 ± 0.003
DecompOpt	-4.839 ± 0.415	-6.874 ± 0.210	-8.425 ± 0.528	0.429 ± 0.011	0.625 ± 0.006
TAGMol	-7.019 ± 0.175	-7.951 ± 0.088	-8.588 ± 0.135	0.553 ± 0.004	0.562 ± 0.003
MolJO	-7.516 ± 0.136	-8.326 ± 0.078	-9.048 ± 0.083	0.556 ± 0.003	0.775 ± 0.003

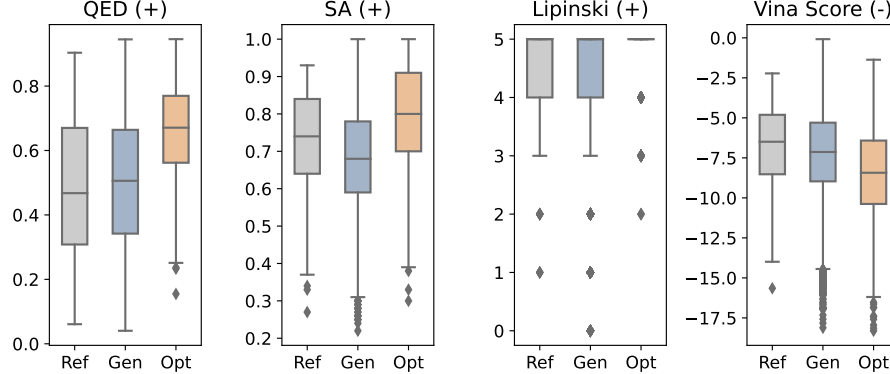


Figure 5. Distribution shift from test set (Ref), backbone without guidance (Gen) to guided MolJO (Opt).

Affinity Analysis. We present the tail distribution of Vina affinities in Table 7, demonstrating that our method not only excels in optimizing overall performance as shown in Fig. 5, but also enhances the quality of the best possible binders.

To better understand the enhanced binding affinities, we further analyze the distribution of non-covalent interactions that are known to play an important role in stabilizing protein-ligand complexes. Fig. 6 demonstrates that the improved affinity results are achieved by forming a greater number of hydrophobic interactions, more hydrogen bond acceptors and π interactions.

Combination of Objectives. In Table 8, we report the results for an exhausted combination of different objectives under the unconstrained setting, where 1000 molecules are sampled in total. It can be seen that combining two objectives yields nearly the best optimized performances for each objective, with the choice of Affinity + SA even displaying improvement in QED. However, from the QED + SA setting, we observe a negative impact on binding affinity. It is possible that

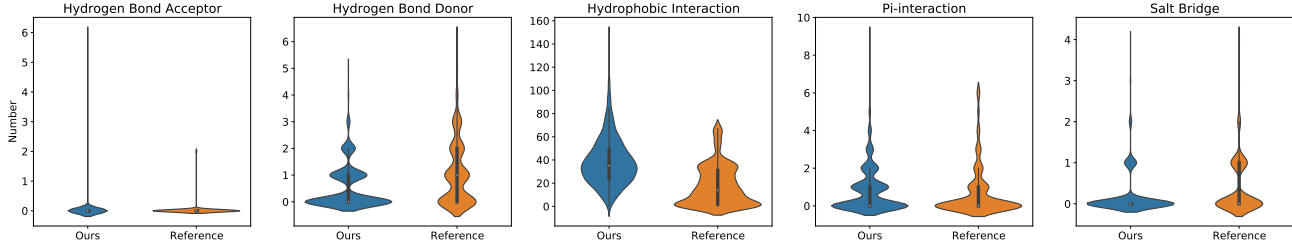


Figure 6. Non-covalent interaction distributions of reference and optimized molecules.

Table 7. Tail distribution of Vina affinities.

	Vina Score 5%	Vina Min 5%	Vina Dock 5%
Reference	-9.98	-9.93	-10.62
AR	-10.05	-10.33	-10.56
Pocket2Mol	-10.47	-11.77	-12.36
TargetDiff	-11.10	-11.57	-11.89
DecompDiff	-10.04	-10.96	-11.77
IPDiff	-12.98	-13.40	-13.63
MolCRAFT	-12.14	-12.34	-12.58
DecompOpt	-10.78	-11.70	-12.73
TAGMol	-13.15	-13.50	-13.67
MolJO	-13.59	-13.90	-14.18

too high a requirement of QED and SA further constrains the chemical space for drug candidates, limiting the types of potential interactions with protein surfaces. When it comes to all objectives, MolJO achieves balanced optimization results, *i.e.* satisfactory QED and SA comparable to single objective optimization or the combination of two, and enhanced affinities compared with the results without affinity optimization, though slightly inferior to the best possible affinity optimization results. This might stem from QED + SA problems described above, suggesting a careful handling of these two objectives. In this regard, we simply choose Affinity + SA objectives in all our main experiments for a clear demonstration of our optimization ability.

For a better understanding of the correlation between objectives, we plot the pairwise relationships for the molecules in the training set in Fig. 7, and calculate the Spearman’s rank coefficient of correlation ρ . The Spearman ρ is 0.41 between SA and QED, and it is reasonable to see such a positive correlation between SA and QED, since these are both indicators of drug-likeness with certain focus and thus alternative to some extent. This aligns with our findings that adopting the Affinity + SA objectives can also benefit QED, and justifies our choice of optimization objectives in this sense. Moreover, although there is also a slightly positive correlation between Vina Score and SA ($\rho = 0.33$), meaning that it is nontrivial to simultaneously optimize both properties, our method succeeds in finding the best balanced combination of properties, demonstrating the superiority of joint optimization compared with TAGMol.

 Table 8. Combinations of different objectives. Top-2 results are highlighted in **bold** and underlined, respectively.

Objective	Vina Score (↓)		Vina Min (↓)		QED (↑)	SA (↑)	Connected (↑)
	Avg.	Med.	Avg.	Med.			
Affinity	-7.74	<u>-7.96</u>	-8.21	-8.19	0.52	0.68	0.87
QED	-6.84	-7.32	-7.54	<u>-7.65</u>	0.66	0.70	0.99
SA	-6.25	-7.24	-7.48	-7.65	0.57	0.78	0.97
QED+SA	-6.55	-7.23	-7.38	<u>-7.52</u>	<u>0.65</u>	0.74	0.99
Affinity+QED	<u>-7.46</u>	-8.04	<u>-8.18</u>	<u>-8.20</u>	0.64	0.67	0.98
Affinity+SA	<u>-7.08</u>	-7.88	<u>-8.05</u>	-8.21	0.57	<u>0.75</u>	0.97
All	-7.09	-7.47	-7.79	-7.76	0.62	0.73	0.98

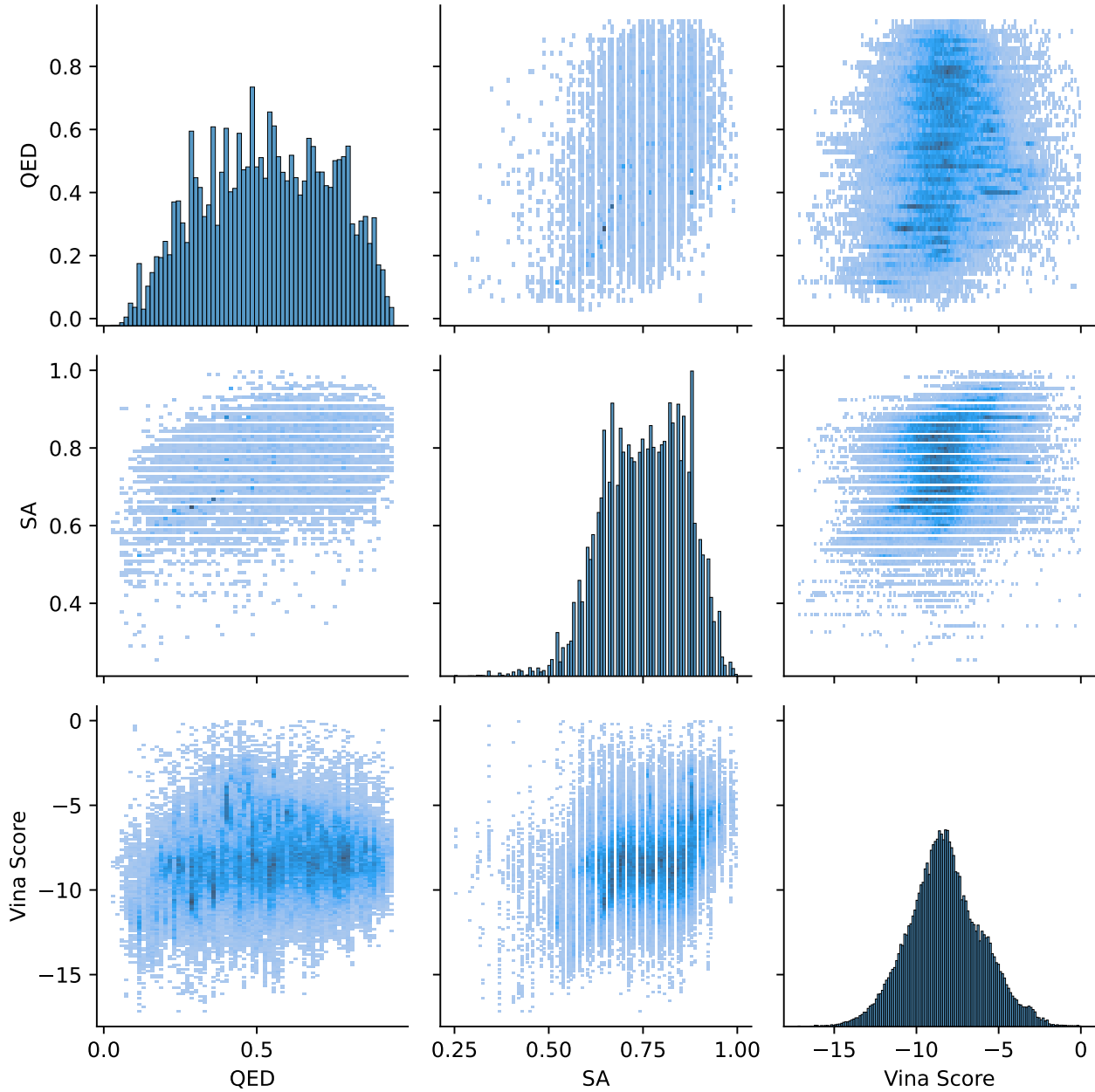


Figure 7. Pairwise correlation of different properties. On the diagonal are histograms showing single property distributions on Cross-Docked2020.

Top-of-N Comparison. We have made the same top-of-N selection ($N = 10$) for picking the top 1/10 from the generated molecules for each baseline. Specifically, for each of the 100 test proteins, a tenth out of roughly 100 molecules are selected based on z -score reranking, where $z = 5 \cdot |norm(\text{Vina})| + norm(\text{QED}) + 1.5 \cdot norm(\text{SA})$, and $norm$ denotes zero mean and unit variance normalization.

This generally shows what the “concentrated space” for desirable drug-like candidates looks like for generative models. As shown in Table 9, our method displays the best Success Rate in top-of-N evaluations, indicating better optimization efficiency. Though IPDiff also displays superior Vina affinities, it comes at the expense of low SA (0.62) and shows only moderate Success Rate, as there is observed to be a slightly positive correlation between Vina Score and SA ($\rho = 0.33$) in Fig. 4, meaning that it is nontrivial to simultaneously optimize both properties. MolJO does a better job in finding the best balanced combination of properties, demonstrating the superiority of gradient-based joint optimization.

Table 9. Top-of-N ($N = 10$) performances for baselines.

Method	Vina Score (↓)		Vina Min (↓)		Vina Dock (↓)		QED (↑)	SA (↑)	Div (↑)	Success Rate (↑)
	Avg.	Med.	Avg.	Med.	Avg.	Med.				
AR	-6.71	-6.35	-7.12	-6.63	-7.81	-7.33	0.64	0.70	0.60	19.1%
Pocket2Mol	-5.80	-5.39	-7.18	-6.50	-8.32	-7.78	0.67	0.84	0.59	40.5%
FLAG	50.37	43.14	6.27	-3.38	-6.57	-6.47	0.74	0.78	0.71	9.6%
TargetDiff	-7.06	-7.57	-8.10	-8.11	-9.31	-9.18	0.64	0.65	0.67	32.6%
DecompDiff	-5.78	-5.82	-6.73	-6.57	-8.07	-8.03	0.61	0.74	0.61	32.1%
MolCRAFT	-7.54	-7.89	-8.40	-8.13	-9.36	-9.05	0.65	0.77	0.63	<u>55.0%</u>
IPDiff	-8.15	-8.67	-9.36	-9.27	-10.65	-10.17	0.60	0.62	0.69	34.6%
MolJO	-8.54	-8.81	-9.48	-9.09	-10.50	-10.14	0.67	0.79	0.61	70.3%

Additional Baselines. For more comprehensive comparison, we have added the results of DiffBP (Lin et al., 2022), D3FG (Lin et al., 2024) and VoxBind (Pinheiro et al., 2024) from a recently proposed benchmark CBGBench (Lin et al., 2025) and concurrent work DecompDPO (Cheng et al., 2025). It can be seen that our MolJO maintains superiority in optimizing the overall properties, reflected by its highest Success Rate.

Table 10. Comparison with additional baselines, where the results for DiffBP, D3FG and VoxBind are calculated based on the samples released by CBGBench, and results for DecompDPO follow the numbers reported by the authors.

Method	Vina Score (↓)		Vina Min (↓)		Vina Dock (↓)		QED (↑)	SA (↑)	Div (↑)	Success Rate (↑)
	Avg.	Med.	Avg.	Med.	Avg.	Med.				
DiffBP	-	-	-	-	-7.34	-	0.47	0.59	-	-
D3FG	-	-	-2.59	-	-6.78	-	0.49	0.66	-	-
VoxBind	-6.16	-6.21	-6.82	-6.73	-7.68	-7.59	0.54	0.65	-	21.4%
DecompDPO	-6.10	-7.22	-7.93	-8.16	-9.26	-9.23	0.48	0.64	0.62	36.2%
MolJO	-7.52	-8.02	-8.33	-8.34	-9.05	-9.13	0.56	0.78	0.66	51.3%

F.2. Ablation Studies

Effect of Joint Guidance. Table 11 shows the effectiveness of joint guidance over coordinates or types. Utilizing gradients to guide both data modalities is consistently better than applying single gradient only, since the energy landscape of a molecular system is a function of both the atom coordinates and the types. Lack of direct control over either modality can lead to suboptimal performance due to not efficiently exploring the chemical space where certain atomic types naturally pair with specific spatial arrangements. Specifically, it can be seen that for affinities, the optimization is closely related to coordinates, while for drug-like properties, simply propagating gradients over coordinates displays no improvement at all. This validates our choice of finding appropriate guidance form jointly, and a single coordinate guidance would be insufficient for generating desirable molecules.

Effect of Backward Correction. We conduct ablation studies regarding the proposed backward correction strategy. w/o Correction denotes sampling θ_i according to Eq. 10. Fig. 8 shows that increasing the steps k in Eq. 12 that have been corrected backward boosts the optimization performance once sufficient past steps are corrected for optimization.

Table 11. Ablation studies of joint optimization for atom types and coordinates, where w/o type means the gradient is disabled for types. Top 2 results are highlighted with **bold** and underlined text.

Objective	Methods	Vina Score (\downarrow)		Vina Min (\downarrow)		QED (\uparrow)	SA (\uparrow)
		Avg.	Med.	Avg.	Med.		
Affinity	Ours	-7.74	-7.96	-8.21	-8.19	0.52	0.68
	w/o type	<u>-7.13</u>	<u>-7.58</u>	<u>-7.82</u>	<u>-7.80</u>	0.50	0.66
	w/o coord	-6.61	-7.23	-7.42	-7.53	0.52	0.71
QED	Ours	-6.84	-7.32	-7.54	-7.65	0.66	0.70
	w/o type	-6.41	-7.03	-7.20	-7.26	0.52	0.67
	w/o coord	-6.50	-7.20	-7.44	-7.42	<u>0.65</u>	0.70
SA	Ours	-6.25	-7.24	-7.48	-7.65	0.57	0.78
	w/o type	-6.29	<u>-6.85</u>	-7.07	-7.09	0.51	0.70
	w/o coord	-6.71	-7.22	-7.60	-7.60	0.57	<u>0.77</u>

It can be inferred that sampling $p_\phi(\theta_i | \theta_{i-1}, \theta_{i-k})$ up until θ_n results in a chain of parameters $\{\theta_{T_i}\}_{i=0}^{\lfloor n/k \rfloor}$, where $T_i = ik + (n \bmod k)$, and $\theta_i \sim p_\phi(\theta_i | \theta_{i-1}, \theta_0)$ when $i \leq (n \bmod k)$.

Smaller number k of corrected steps moves the starting point θ_{T_0} closer to θ_0 and sees more updates along the chain. We observe that when k is too small, the sampling process tends to suffer from error accumulation instead of error correction due to stochasticity. Once k is larger than 50, the process is better balanced in exploiting the shortcut (*i.e.* interval k) and exploring the stochasticity to reduce approximation errors via a few updates (*i.e.* $\lfloor n/k \rfloor$). The final k is set to 130, while our strategy is robust within the range $k \in (50, 200]$.

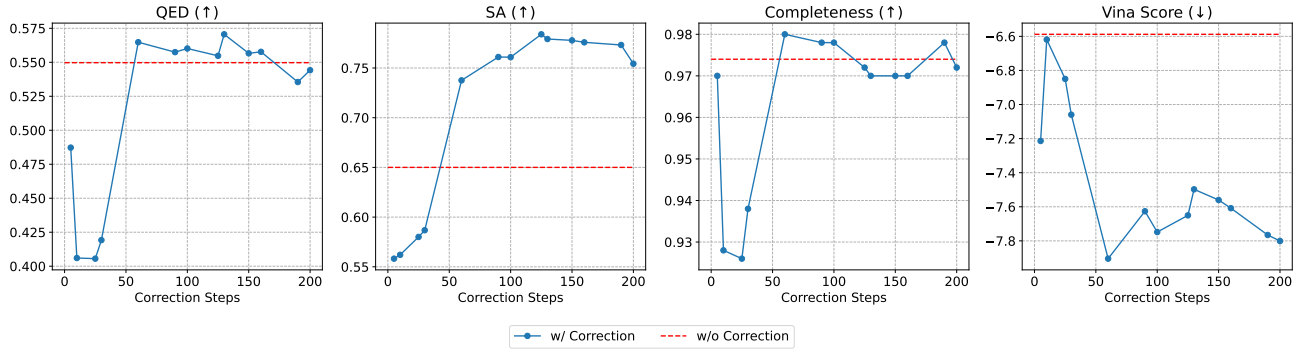


Figure 8. Ablation study of backward correction. Correction Step on the x-axis means the length of history k , and w/o Correction means vanilla update ($k = 1$) with a Monte-Carlo estimate of y .

Additionally, we have conducted pairwise t-tests comparing our guided Backward Correction ($k = 130$) approach against both Vanilla ($k = 1$) and SDE guidance. The results in Table 12 show statistically significant improvements ($p < 0.05, N = 1000$) for our proposed strategy.

Table 12. P-values for pairwise t-tests.

p-value	Vina Score	Vina Min	Vina Dock	SA	QED
Ours vs. Vanilla	2.63E-13	3.31E-31	2.79E-35	8.10E-115	1.98E-26
Ours vs. SDE	2.55E-19	6.48E-19	7.84E-4	2.10E-50	1.82E-12

Effect of Scales. We conduct a grid search of guidance scales, and report the full results of ablation studies on different guiding scales within the range $\{0.1, 1, 10, 20, 50, 100\}$ for different objectives (Affinity, QED, SA) in Table 13, where 10

molecules are sampled for each of the 100 test proteins.

For binding affinity, the optimization performance steadily improves with increasing scales, but the ratio of complete molecules significantly decreases when the scale is greater than 50.

For QED and SA, MolJO achieves best results when the scale is around 20 and 50.

In order to maintain the comparability with molecules without guidance, we stick to the scale range where the connected ratio remains acceptable, and therefore set the guidance scale to 50 for all our experiments.

Table 13. Full ablation studies on different guiding scales for different objectives. Top-1 values are highlighted in **bold**.

Objective	Scale	Vina Score (↓)		Vina Min (↓)		QED (↑)	SA (↑)	Connected (↑)
		Avg.	Med.	Avg.	Med.			
Affinity	0.1	-6.28	-6.98	-7.17	-7.25	0.50	0.70	0.96
	1	-6.24	-7.01	-7.27	-7.29	0.50	0.69	0.96
	10	-6.69	-7.46	-7.46	-7.67	0.51	0.70	0.97
	20	-7.03	-7.87	-7.84	-8.08	0.51	0.70	0.98
	50	-7.64	-8.38	-8.39	-8.64	0.53	0.68	0.90
	100	-9.33	-9.55	-9.87	-9.85	0.55	0.63	0.55
QED	0.1	-6.03	-6.92	-7.10	-7.19	0.51	0.70	0.97
	1	-6.24	-7.09	-7.31	-7.31	0.56	0.71	0.96
	10	-6.12	-7.07	-7.29	-7.41	0.66	0.71	0.98
	20	-6.33	-7.23	-7.34	-7.64	0.66	0.69	0.98
	50	-6.84	-7.32	-7.54	-7.65	0.66	0.70	0.99
	100	-6.25	-6.83	-7.02	-7.10	0.62	0.60	0.95
SA	0.1	-6.30	-7.11	-7.19	-7.29	0.50	0.70	0.96
	1	-6.17	-7.16	-7.36	-7.37	0.52	0.73	0.97
	10	-5.87	-7.23	-7.39	-7.72	0.57	0.78	0.98
	20	-6.14	-7.24	-7.49	-7.72	0.56	0.79	0.98
	50	-6.38	-7.29	-7.86	-7.77	0.54	0.79	0.99
	100	-6.08	-7.36	-7.51	-7.85	0.54	0.78	0.98

G. Evaluation of Molecular Conformation

PoseCheck Analysis. To measure the quality of generated ligand poses, we further employ PoseCheck (Harris et al., 2023) to calculate the Strain Energy (**Energy**) of molecular conformations and Steric Clashes (**Clash**) w.r.t. the protein atoms in Fig. 9 and 10, respectively.

Our proposed MolJO not only significantly outperforms the other optimization baselines in both Energy and Clash, but also shows competitive results with strong-performing generative models, in which Pocket2Mol achieves lower strain energy via generating structures with fewer rotatable bonds as noted by Harris et al. (2023), and fragment-based model FLAG directly incorporates rigid fragments in its generation. As for clashes, we achieve the best results in non-autoregressive methods.

Notably, IPDiff ranks the least in Strain Energy and displays severely strained structures despite its strong performance in binding affinities. This arguably suggests that directing utilizing pretrained binding affinity predictor as feature extractor might result in spurious correlated features, even harming the molecule generation.

RMSD Distribution. We report the ratio of redocking **RMSD** below 2Å between generated poses and Vina docked poses to reveal the agreement of binding mode. Due to issues of poses generate by Autodock, not all pose pairs are available for calculating symmetry-corrected RMSD, where we report the non-corrected RMSD instead to make sure that all samples are faithfully evaluated. As shown in Fig. 11, the optimization methods all display a tendency towards generating a few outliers, which might be attributed to the somewhat out-of-distribution (OOD) nature of optimization that seeks to shift the original distribution. Among all, DecompOpt generates the most severe outliers with RMSD as high as 160.7 Å, and its unsatisfactory performance is also suggested by the lowest ratio of RMSD < 2Å (24.3%), while for gradient-based TAGMol and our method, it only has a negligible impact and the ratio is generally more favorable.

Overall Conformation Quality and Validity. The overall results in Table 14 show that our gradient-based method actually improves upon the conformation stability of backbone in terms of energy and clash, demonstrating its ability to faithfully model the chemical environment of protein-ligand complexes, while DecompOpt generates heavily strained structures similar to DecompDiff, and TAGMol ends up with even worse energy than its backbone TargetDiff. Moreover, from the perspective of validity reflected by **Connected Ratio**, the optimization efficiency of RGA and DecompOpt is relatively low as suggested by the ratio of successfully optimized molecules.

Ring Size. For a comprehensive understanding of the effect of property guidance, we additionally report the distribution of ring sizes in Table 15, showing that the gradient-based property guidance generally favors more rings, but our result still lies within a reasonable range, and even improves upon the ratio of 4-membered rings.

Table 14. Summary of conformation stability results. Energy, Clash are calculated by PoseCheck. Connected is the ratio of successfully generated valid and connected molecules.

	Energy Med. (↓)	Clash Avg. (↓)	RMSD < 2Å (↑)	Connected (↑) ¹
Reference	114	5.46	34.0%	100%
AR	608	4.18	36.5%	93.5%
Pocket2Mol	186	6.22	31.3%	96.3%
FLAG	396	40.83	8.2%	97.1%
TargetDiff	1208	10.67	31.0%	90.4%
DecompDiff	983	14.23	25.1%	72.0%
IPDiff	5861	10.31	17.9%	90.1%
MolCRAFT	196	6.91	42.4%	96.7%
RGA	-	-	-	52.2%
DecompOpt	861	16.6	24.3%	2.64%
TAGMol	2058	7.41	37.2%	92.0%
Ours	163	6.72	43.5%	97.3%

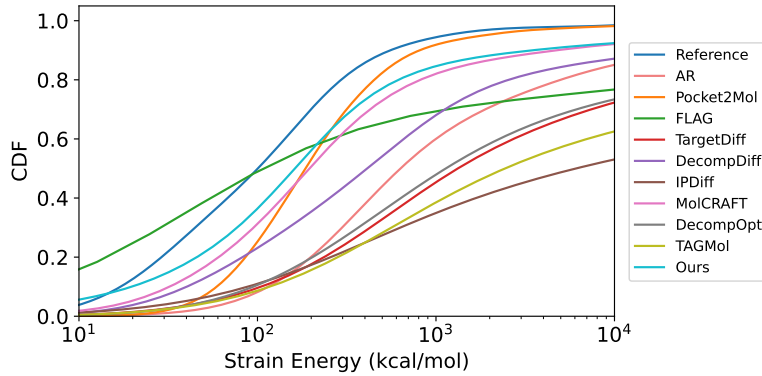


Figure 9. Cummulative density function (CDF) for strain energy distributions of generated molecules and reference molecules.

H. Inference Time

We report the time cost in Table 16 for optimization baselines in the table below, which is calculated as the time for sampling a batch of 5 molecules on a single NVIDIA RTX 3090 GPU, averaged over 10 randomly selected test proteins.

¹Connected ratio of DecompOpt and RGA is calculated based on the optimization results of all rounds provided by the authors. For each of the N rounds, a total of k molecules ought to be generated, thus we divide the total number by $N \times k \times n$.

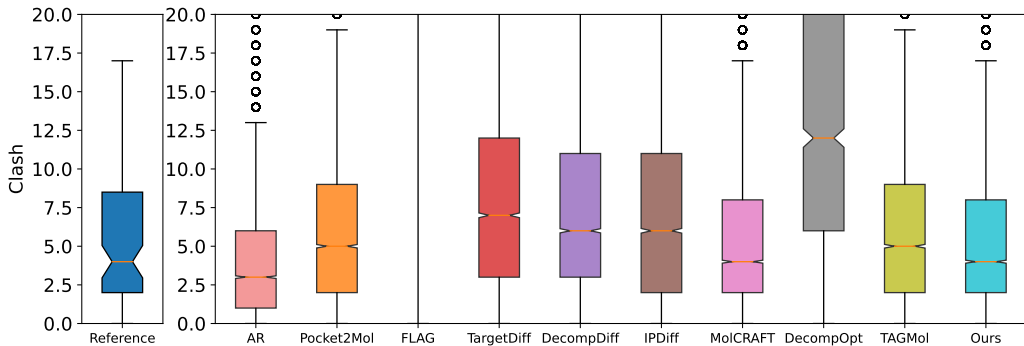


Figure 10. Box plot for clash distributions of generated molecules and reference molecules.

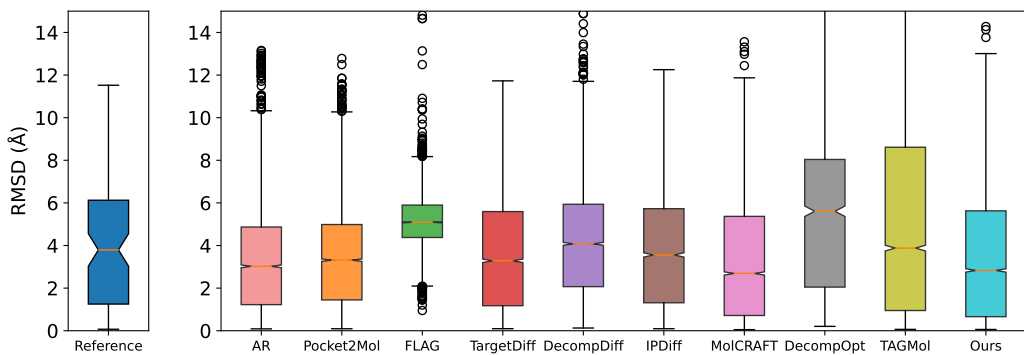


Figure 11. Boxplot for RMSD distributions of generated molecules and reference molecules.

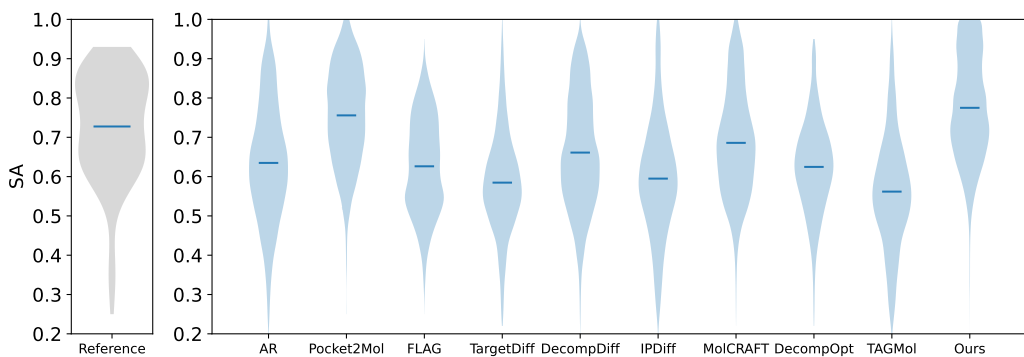


Figure 12. Violin plot for SA distributions of generated molecules and reference molecules.

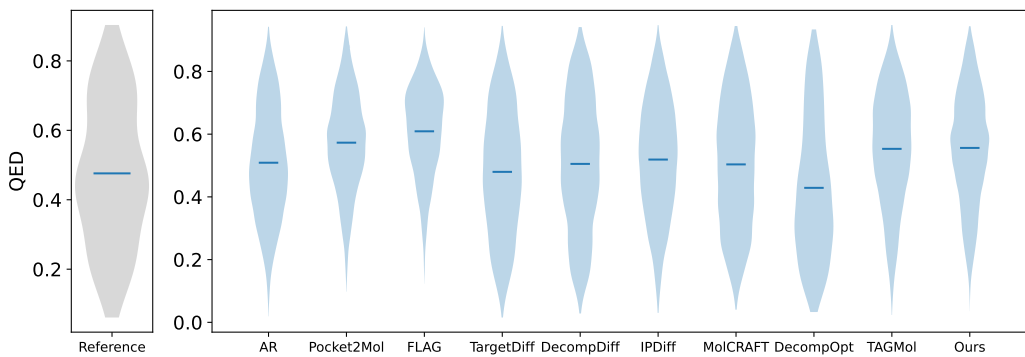


Figure 13. Violin plot for QED distributions of generated molecules and reference molecules.

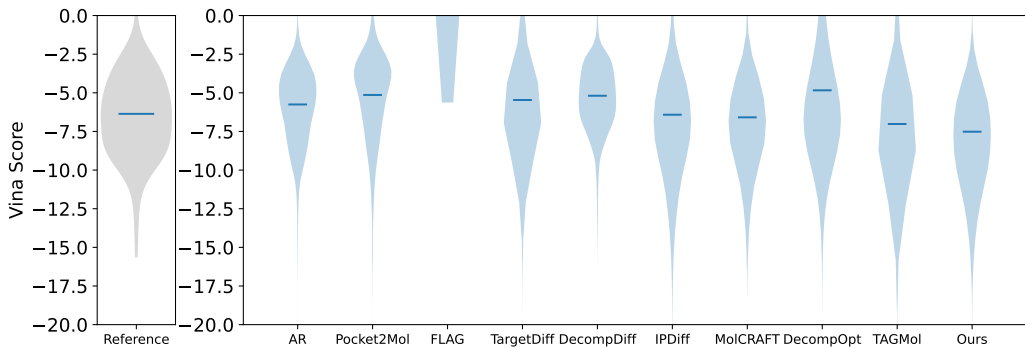


Figure 14. Violin plot for Vina Score distributions of generated molecules and reference molecules.

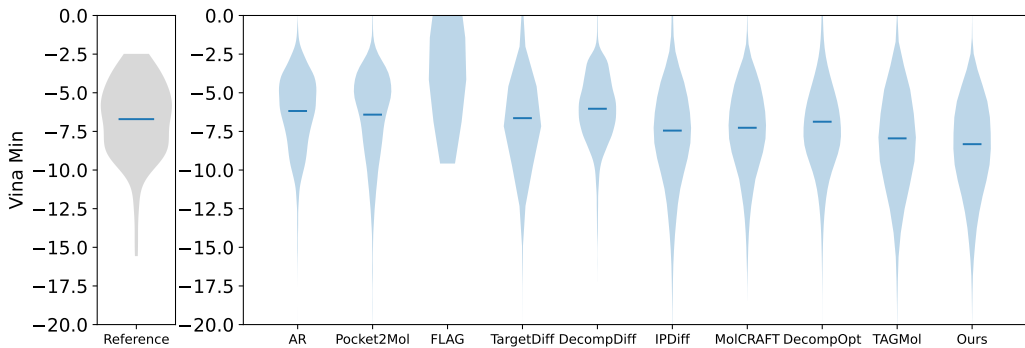


Figure 15. Violin plot for Vina Min distributions of generated molecules and reference molecules.

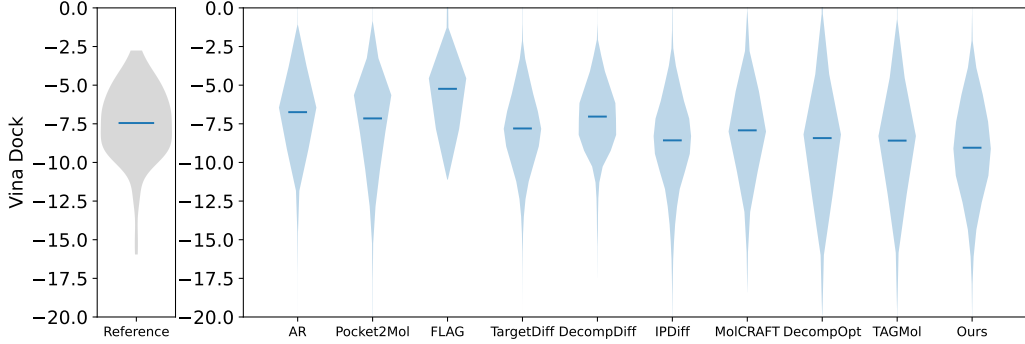


Figure 16. Violin plot for Vina Dock distributions of generated molecules and reference molecules.

Table 15. Proportion (%) of different ring sizes in reference and generated ring structured molecules, where 3-Ring denotes three-membered rings and the like.

	#Rings Avg.	3-Ring	4-Ring	5-Ring	6-Ring
Reference	2.8	4.0	0.0	49.0	84.0
Train	3.0	3.8	0.6	56.1	90.9
AR	3.2	50.8	0.8	35.8	71.9
Pocket2Mol	3.0	0.3	0.1	38.0	88.6
FLAG	2.1	3.1	0.0	39.9	84.7
TargetDiff	3.1	0.0	7.3	57.0	76.1
DecompDiff	3.4	9.0	11.4	64.0	83.3
IPDiff	3.4	0.0	6.4	51.0	83.7
MolCRAFT	3.0	0.0	0.6	47.0	85.1
DecompOpt	3.7	6.8	11.8	61.4	89.8
TAGMol	4.0	0.0	8.5	62.5	82.6
MolJO (Aff)	3.6	0.0	0.4	46.7	92.5
MolJO (QED)	3.7	0.0	0.5	58.0	96.1
MolJO (SA)	3.8	0.0	0.2	37.0	97.8
MolJO (Aff+SA)	3.9	0.0	0.1	37.0	98.1
MolJO (All)	3.6	0.0	0.3	44.4	97.6

Table 16. Inference time cost of optimization baselines, error bars indicating the standard deviation across 10 randomly selected proteins.

Model	Ours	TAGMol	DecompOpt	RGA	AutoGrow4
Time (s)	146 ± 11	667 ± 69	11714 ± 1115	458 ± 43	2586 ± 360

I. More Related Works

General Molecule Optimization. As an alternative to target-aware generative modeling of 3D molecules, the optimization methods are goal-directed, obtain desired ligands usually by searching in the drug-like chemical space guided by property signals (Bilodeau et al., 2022; Sun et al., 2023; Du et al., 2024). General optimization algorithms were originally designed for ligand-based drug design (LBDD) and optimize common molecule-specific properties such as LogP and QED (Olivecrona et al., 2017; Jin et al., 2018; Nigam et al., 2020; Spiegel & Durrant, 2020; Xie et al., 2021; Bengio et al., 2021), but could be extended to structure-based drug design (SBDD) given docking oracles. However, since most early attempts did not take protein structures into consideration thus were essentially not target-aware, it means that they need to be separately trained on the fly for each protein target when applied to pocket-specific scenarios. RGA (Fu et al., 2022) explicitly models the protein pocket in the design process, overcoming the transferability problem of previous methods. DiffAC (Zhou et al., 2024b) utilizes policy gradients for SDEs to fine-tune pretrained diffusion models given affinity signal, demonstrating the potential of RL method but limited to Vina Score optimization only.

Constraint Molecule Optimization. Real-world lead optimization typically requires retaining specific substructures to preserve critical molecular interactions or properties. Recently, CBGBench (Lin et al., 2025) introduces a generative graph completion framework for systematic evaluation, including tasks such as linker design, fragment growing, side chain decoration, and scaffold hopping, showing the potential for rigorous benchmarking of structure-based molecular optimization under predefined substructural constraints.